

## Article

# Experimental and Numerical Study of Novel Vortex Bladeless Wind Turbine with an Economic Feasibility Analysis and Investigation of Environmental Benefits

Hasan Hamdan <sup>1</sup>, Sharul Sham Dol <sup>1,\*</sup>, Abdelrahman Hosny Gomaa <sup>1</sup>, Aghyad Belal Al Tahhan <sup>1</sup>, Ahmad Al Ramahi <sup>1</sup>, Haya Fares Turkmani <sup>1</sup>, Mohammad Alkhedher <sup>1</sup> and Rahaf Ajaj <sup>2</sup>

<sup>1</sup> Department of Mechanical and Industrial Engineering, Abu Dhabi University, Abu Dhabi P.O. Box 59911, United Arab Emirates; 1065775@students.adu.ac.ae (H.H.); 1066731@students.adu.ac.ae (A.H.G.); 1070819@students.adu.ac.ae (A.B.A.T.); ahmad.alramahi@adu.ac.ae (A.A.R.)

<sup>2</sup> Department of Environmental & Public Health, Abu Dhabi University, Abu Dhabi P.O. Box 59911, United Arab Emirates; rahaf.ajaj@adu.ac.ae

\* Correspondence: sharulshambin.dol@adu.ac.ae

**Abstract:** This study combines experimental and numerical evaluations of Vortex Bladeless Wind Turbines (VBWTs) to understand their potential in renewable energy generation. The methodology employs Two-Way Fluid–Solid Interface (FSI) simulations, alongside real-world data, providing important insights into the turbine’s vibration dynamics and flow interactions during operation. Key findings include identifying optimal vibration frequencies and amplitudes that enhance energy harvesting and a clear advantage in power-generation estimations shown by one of the models used. The study reveals possible applications of VBWT in various settings like airport runways, highways, and buildings, indicating a promising avenue for incorporating such renewable-energy solutions. Discussions on the economic feasibility and environmental benefits of VBWT deployment are also presented, suggesting a need for further research and optimization in this area. A conceptual generator design and business model are introduced as part of a broader discussion on technology integration and energy storage. The research in this study encompasses experimental and numerical analysis, to achieve a broader understanding of the workings of a VBWT, realizing the feasibility of using such systems in lower-wind-speed conditions and upscaling to higher-wind-speed cases.

**Keywords:** vortex bladeless; vortex generator; wind energy; CFD; aerodynamics



**Citation:** Hamdan, H.; Dol, S.S.; Gomaa, A.H.; Tahhan, A.B.A.; Al Ramahi, A.; Turkmani, H.F.; Alkhedher, M.; Ajaj, R. Experimental and Numerical Study of Novel Vortex Bladeless Wind Turbine with an Economic Feasibility Analysis and Investigation of Environmental Benefits. *Energies* **2024**, *17*, 214. <https://doi.org/10.3390/en17010214>

Academic Editor: Davide Astolfi

Received: 21 November 2023

Revised: 26 December 2023

Accepted: 28 December 2023

Published: 30 December 2023



**Copyright:** © 2023 by the authors. Licensee MDPI, Basel, Switzerland. This article is an open access article distributed under the terms and conditions of the Creative Commons Attribution (CC BY) license (<https://creativecommons.org/licenses/by/4.0/>).

## 1. Introduction

In recent years, renewable energy (RE) has become widely discussed among experts and the general public [1]. The growing world population is causing an increase in energy demand, which puts additional pressure on traditional energy sources to meet the rising consumption needs [2]. Since the early 1970s, fossil fuel depletion and climate change consequences have been related to climate change [1].

As a result, numerous countries have adopted renewable energy sources (RESs) to reduce their reliance on fossil fuels and other non-renewable sources [3]. The International Energy Agency predicts that renewable energy sources (RESs) will need to rapidly increase in the electrical industry to achieve a sustainable future [4]. There has been a focus on technological advancements to address this issue in the Middle East and North Africa (MENA) countries, where freshwater resources are scarce and there is a rapidly growing population. This has led to cost-effective solutions utilizing renewable energy technologies for desalination processes [5]. According to Hassan et al. [4], the MENA region is often considered a desert area, which makes freshwater scarcity a significant issue. It is vital to strengthen energy security to improve water resource management and security. Solar

and wind energy are the focus of renewable energy sources (RESs). Although RESs are intermittent, they are the most promising option for meeting future energy needs. As a result, various policy options are necessary to encourage the use of renewable energy.

RESs mainly consists of solar, wind, hydropower, geothermal, and biomass [6]. The increasing attraction towards RES is because of its environmentally friendly nature and sustainability, emitting either zero or almost-zero air pollutants and greenhouse gases (GHGs) [7]. While renewable energy resources are clean and readily available options, their implementation can pose challenges, such as high capital costs and storage-system efficiency issues [8]. Researchers are working on developing micro-grid hybrid power systems that utilize multi-objective optimization techniques [3]. These systems allow for energy storage solutions that can absorb energy from variable renewable sources and generate electricity during peak periods at a lower cost. This approach can significantly aid in integrating intermittent renewable energy into existing power systems [4,9].

Wind energy (WE) is a great eco-friendly, clean option with a minimum land requirement and no greenhouse gas emissions [10]. Adopting eco-friendly technologies like WE is crucial for our future [11]. However, depending on variable weather conditions, significant changes in zonal climate and the water cycle, and complications with energy storage systems make it a challenging and costly mission [3]. Wind turbines cannot produce the desired energy annually, due to high cut-in and cut-off wind speeds that force them to go into standby mode. As the world aims to keep the rise in temperature below 2 °C, authorities, companies, and system integrators are looking for ways to manage intermittent energy production from renewable energy sources (RESs) while still meeting environmental goals [4,11]. To address this challenge, it is crucial to connect intermittent energy sources with dispatchable ones, such as hybrid renewable energy systems (HRESs), which can include at least two different RESs and non-renewable sources. Integrating wind and solar energy in a hybrid system can increase overall energy production and mitigate energy alteration caused by RE [3]. System design, size optimization, and performance assessment are significant considerations for HRES, and optimizing system size is essential to minimize costs while maximizing performance. Modern techniques are more popular than classical algorithms, and include software tools [12].

While RES, like wind energy, offers many benefits, it is important to note that relying on these technologies can make it challenging to estimate power consumption. This can lead to adjusting how energy supplies are distributed and controlled on the grid, which can cause issues. To meet the increasing market demand, more work is needed, especially from the non-government sector, to invest in infrastructure and research funding for development. This was noted by Hassan et al. in 2023 [4].

The growing demand for renewable energy sources has inspired researchers and engineers to explore recent technologies to achieve highly efficient renewable energy applications. Wind energy is one of the most common renewable energy sources used in industry. It is a renewable and sustainable source of energy that has been harnessed over the years through multiple forms of technologies and devices. The most common methods for wind energy harvesting are rotational and oscillation wind harvesting. The rotational wind harvesting involves the traditional large-span blades that rotate and generate electricity at varying wind speeds, such as the traditional horizontal axis wind turbines, and the vertical axis wind turbine, which has been previously researched numerically by Pervaiz et al. [13] to optimized it and to understand its performance under different conditions, but the fact remains that these two configurations require sufficient wind speeds to operate. However, oscillation wind harvesting has been studied for the past couple of years [14–16]. In this method, a small wind gust flowing over a body is disturbed by the body creating turbulence downstream. Thus, the body begins to shed vortices which cause uneven pressure distribution, which causes the body to oscillate or vibrate due to changing aerodynamic forces [17]. Eventually, when the natural frequency of the body matches the vortex-shedding frequency, the body will resonate. This will amplify its movement, i.e., vibration. This phenomenon is referred to as resonance, which forms the basis of the operational principle of Vortex Blade-

less Wind Turbines (VBWTs). This technology has been a subject of interest in worldwide research and development. However, it is still important to understand the underlying mechanisms and principles that govern its motion, for future developments. The main principle behind the operation of the VBWT is the vortex-induced vibration phenomena [18,19]. Furthermore, VBWT technology stands out as a revolutionary approach to wind energy, where it leverages the vibrations generated by the oscillation of the system to convert wind energy into usable power. As described earlier, the oscillation of the turbine occurs due to the vortex-shedding phenomenon. However, when the frequency of the shedding becomes aligned with that of the VBWT natural frequency, a phenomenon known as the lock-in region is observed. In this region, the system oscillates synchronously with the shedding frequency of the system. Thus, the occurrence of this phenomenon extends the vibration bandwidth of the VBWT. It is safe to assume that, within the lock-in region, the maximum energy can be extracted from the turbine. However, it is also important to understand the influence and theory behind the main contributing phenomenon to the VBWT technology, which is the vortex-induced vibration (VIV) and vortex shedding [15,20].

Vortex-induced vibration (VIV) is observed when a bluff body induces vibrations or oscillatory motion, due to vortex shedding. There are two critical factors to consider when analyzing the influence of this phenomenon: vortex-shedding frequency  $f_s$ , and vortex wake formation. The principle of wake formation behind a bluff body was first introduced by Karman [21]. In his research, it was observed that the ideal arrangement of an infinite double row of vortices during an inviscid flow is stable for any range of displacement. Similarly, Berman et al. [22] characterize a bluff body as a body that generates a separated flow over a substantial area of its surface inside a fluid stream. Additionally, the mechanics of the vortex formation and vortex regions were described by Gerrard [23]. In his model, the mutual interaction between the shear layers is a critical factor in the inducement and formation of a vortex street. He postulated three conditions under which the particles in an opposing shear layer are drawn toward the wake region. This is observed in Figure 1.

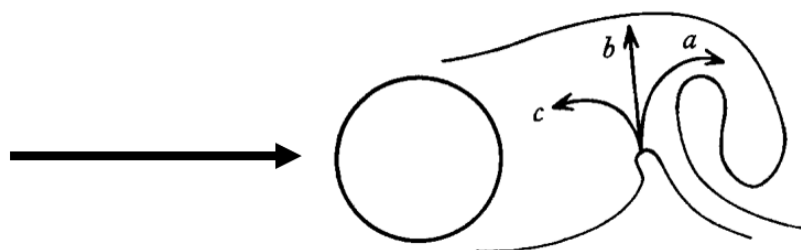


**Figure 1.** The conditions under which fluid particles are drawn into the wake region. (a) The particles can be introduced to the growing region, and reduce their strength. (b) They can enter the shear layer and have positively- and negatively-signed vorticity. (c) They can be re-inserted into the near-wake region [23].

Several factors influence the airflow over a cylindrical body. These factors include surface roughness  $\epsilon$ , flow perturbation, Reynolds number ( $Re$ ), and the geometry of the body in general. Body geometry has a significant impact on the flow separation at different angles of the body. For example, the bluffer the body, the more drag it will induce, and thus, a lower vortex-shedding frequency will be observed. In a previous analysis of bluff bodies, Su et al. [24] reported galloping vibration on asymmetric cross-sections. Furthermore, studies highlighted the significance of this phenomenon combined with VIV to generate large fluctuations [25]. Furthermore, an important relation has been established between the wake width and the vortex-shedding frequency, and that is known as the universal Strouhal number  $S_t$ , which has a value of 0.2. However, the mathematical relation defining it can be written as:

$$S_t = \frac{f_s D}{U} \quad (1)$$

where  $f_s$ ,  $D$ , and  $U$  are the shedding frequency, the body diameter, and the inlet velocity, respectively; thus, from the relation in Equation (1), it is important to emphasize the concept of vortex shedding. As previously discussed, vortex shedding is of significant importance in the field of fluid mechanics. This is observed during the passage of a flow around a bluff or cylindrical body, thus causing the flow on either side of the body to oscillate and shed alternating vortices. This shedding is observed through a pattern known as the Von Karman Vortex Street. Additionally, the vortex pattern of a flow is dependent on Reynold's number. It is observed that the pure Karman Street pattern is observed at  $Re$  ranges between 80 and 300 [26]. Therefore, in this study, we will consider the influence of geometry on the nature of the flow pattern, given the dependence of the Reynolds number on the diameter  $D$  of the cylindrical body. However, other turbulence characteristics can still be researched to understand the flow around a flexible cylindrical or semi-cylindrical structure, such as the irregularity, diffusivity, and rationality of the flow, and this was previously investigated by Dol et al. [27], to understand the mixing of fluids around flexible cylindrical structures.

The introduction of these concepts is important when designing bladeless wind turbines (BWTs), especially cylindrical-shaped structures. As reported by Khalak and Williamson [28], the reduction in the velocity significantly influences the dynamic response of a flexible cylinder. Additionally, the variation in the Reynolds number has a considerable influence on the maximum amplitude of a rigid cylinder, due to the changes it dictates on the flow regime surrounding the body [25]. As the  $Re$  increases, the flow transitions from laminar to turbulent, as described by classical fluid mechanics. Therefore, this induces a broader spectrum of vortex-shedding frequency which causes stronger interactions with the cylinder's natural frequency, eventually, increasing the vibrational amplitude of the body. Figure 2 shows one of the many designs of bladeless-wind-turbine systems in the literature, in which most opt for a cylindrical shape supported by a flexible-rod mechanism. This design approach has recently been regarded as a semi-standard way of designing a BWT; however, improvements can be made to the working of BWTs by not only exploring the alterations of the design, but also by implementing or adding structures or mechanisms to the surface of the BWT to enhance the aerodynamics, thus enhancing the power generation potential of the system.

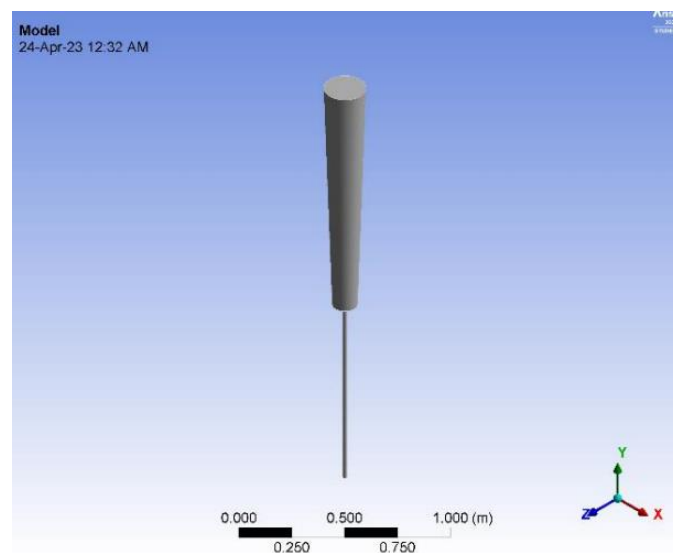


**Figure 2.** Existing design and work on a Bladeless Wind Turbine System carried out by [29].

The size of the generated wake behind the body is important in VBWT applications. This is because generating a substantial amount of power from VBWTs requires multiple VBWT systems to be arranged in an array arrangement with calculated spacing, such that the wake of one system does not interfere with the upstream flow of the other systems. The

multiple-cylinder arrangement and center spacing are key factors when designing multiple oscillating-cylindrical systems, as described by [30,31].

Recently, the VBWT industry began to witness significant growth in both research and development. However, there are still many challenges to be addressed in this field. Gohate et al. [32] highlighted the VIV concept as a method for wind energy harvesting, in which we can observe a detailed description of all the physical concepts associated with it. Additionally, various concepts associated with VBWT technology have been explained by [33], while shedding light on several types of thread attached to mast models. Aghazadeh et al. [34] emphasized the taper ratio of tapered cylindrical masts that could maximize the induced vorticity in VBWT systems. Additionally, Samy et al. [35] performed a complete design study on the usage of vortex generators in amplifying the effects of VIV in VBWT. Furthermore, Elsayed and Farghaly [36] presented a theoretical and numerical analysis and design of a VBWT, where they calculated the forces affecting the performance of the turbine and concluded that the results obtained by their numerical approach can be utilized for the practical design of VBWTs at low wind speeds. Additionally, numerous studies have been conducted to optimize the design of VBWTs. A straightforward design was presented by Akaydin et al. [37]. In their design, the model was a cylinder 0.203 m high and 0.0198 m in diameter. This simple model could generate 0.1 mW of electrical power. On the other hand, the feasibility of arc-and disc-shaped pendulums for VBWTs, which generated around 1.5 W of power at a wind speed of 4.63 m/s, was analyzed by Salvator et al. [38]. Similarly, more recent research by [39] emphasized the benefits of controlling the oscillations of the cylinders on the enhancement of the performance of VBWT at varying low wind speeds. Francis et al. [40] provided a comparative analysis of the displacement and vibrational frequency of cylindrical tapered VBWT geometries with different building materials. Therefore, we can observe that there is an ongoing effort to analyze and optimize the performance and overall power generation of VBWT.

In this study, we conduct a thorough analysis on the flow behavior over a novel Vortex Bladeless Wind Turbine (VBWT) design. The design incorporates the specific shaped vortex generators, scattered in a specific distribution along the surface of the mast. Furthermore, a computational fluid dynamics (CFD) analysis was used to study the fluid flow behavior around the VBWT structure, and a transient structural analysis was conducted through two-way fluid–solid interface (FSI) coupling, to observe the vortex shedding and induced vibration on the proposed VBWT design; here, both the implemented models (CFD and FSI) are used together, to understand the strength of wake structures and fluid circulation, which was researched in a previous study by Dol and Chan [41]. Additionally, two different configurations of VBWT models were analyzed at similar flow conditions, to observe optimal designs. Moreover, the fluid flow pattern, vorticity, and wake characteristics were analyzed, along with velocity and displacement analysis. The structures proposed are later discussed in Section 2.

## 2. Methodologies

Designing an accurate CFD study requires following appropriate procedures and modeling strategies. In this section, we provide a comprehensive exposition of the analytical techniques and approaches followed in this study. The simulation methodology utilized CFD and transient structural analysis, which are coupled and facilitated through two-way FSI. This approach is followed to ensure an accurate representation of the interactions between the flowing air and the VBWT. This section primarily comprises three distinct phases of the simulation study, i.e., CFD analysis, transient structural study, and FSI-coupling analysis. In these phases, we thoroughly discuss the employed setting, boundary conditions, and the governing equations of each phase.

### 2.1. Design and Components of the VBWT

The typical Vortex Bladeless Wind Turbine (VBWT) consists of around six main components, which makes it a complete power-generation system. To increase the stiffness of the proposed VBWT, a linearly tapered mast is proposed. This is done to create a non-uniform mass distribution along the longitudinal axis of the VBWT. The reason we focused on increasing the stiffness of the mast is that a high-stiffness mast can produce higher natural frequencies, as proposed by [42]. Distinct types of tapered masts can be observed in the literature. However, our proposed design conforms to an inverted version of the models investigated by [42].

Our model utilizes an inverted version of the models studied by [42], having a larger diameter on the top and a smaller diameter on the bottom part of the mast. This is done to ensure that the larger diameter exposes a bigger surface area to the wind flow, thus maximizing the vortex shedding and increasing the oscillations generated by the mast. The effect of the increased shedding generates a stronger FSI force between the flowing wind and the VBWT. These forces are then transferred down to the bottom region of the mast, where the energy conversion mechanism is housed. Furthermore, having a relatively smaller diameter of the mast at the bottom stabilizes the turbine and focuses the load transfer efficiently. Eventually, the effective load transfer within the mast can amplify the effect of resonance along the mast. The proposed designs are illustrated in Figure 3.

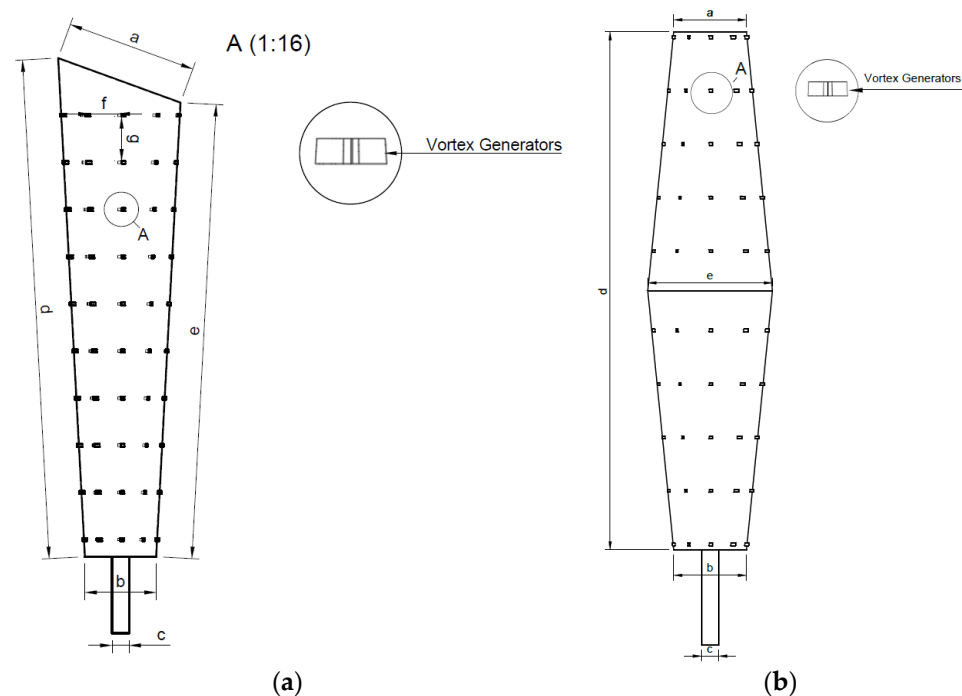


**Figure 3.** Proposed VBWT designs with vortex generators for this study: (a) Model 1 (b) Model 2.

The second feature of the proposed model is highlighted through a detailed projection of the vortex generators (VG), as observed in both models of Figure 3. These VGs are placed in a specified spacing along the surface of the mast, and are scattered to cover the whole mast. These VGs are implemented to enhance the vortex-shedding effect and the vorticity formation around the VBWT. Finally, the base is designed as a square structure to introduce stability and maintain the support for the lower part of the mast. A typical VBWT system consists of all the components illustrated in Figure 4, retrieved from [43].

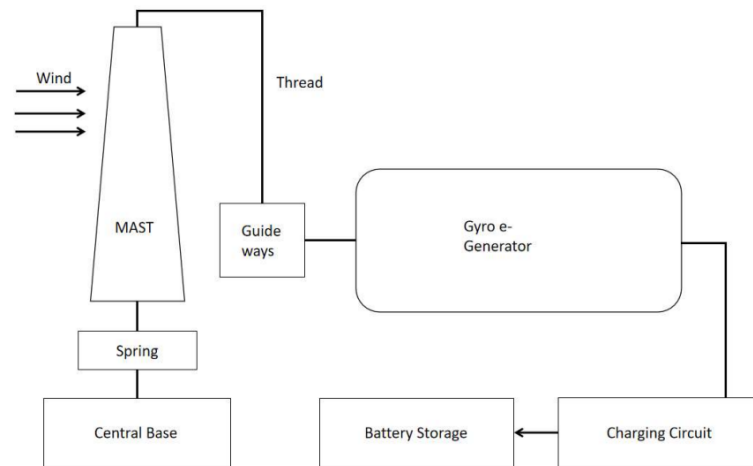


**Figure 4.** Schematic of a VBWT wind-energy-harvesting system [43].

## 2.2. Spring-System Selection and Design

Springs are frequently made to lessen or dampen vibrations. But, in bladeless wind turbines, the goal is to enhance vibrations, rather than to dampen them. The desired deflection, applied load, spring material, stiffness, and configuration of the spring system must all be carefully considered when designing an ideal spring for a bladeless wind turbine. The mass-spring system and cantilever arrangement stand out as practical possibilities among the various spring arrangements which are accessible, including the parallel-spring arrangement, torsional-spring design, and cantilever arrangement. Since there are not many moving elements, these arrangements are employed for their simplicity and dependability. This contributes to greater longevity and less maintenance. Additionally, because of their adaptability, the mass-spring system and cantilever arrangement can be modified to meet a variety of operating situations and performance standards. These spring configurations can be designed for each installation, whether it be a smaller domestic bladeless wind turbine or a larger commercial one, to ensure optimum performance. The mass-spring system's and cantilever arrangement's capacity to regulate vibrational frequencies is one of their advantages. A particular frequency of interest can be matched by varying the spring's stiffness. For the energy-conversion process to be maximized and the turbine's power generation to be optimized, vibrational frequencies must be controlled. Arranging the spring can be carried out in a way that amplifies the deformation for the longest time and decreases the deformation angle, to increase the power produced. The following equations govern the principles of design and selection of the specific spring system for the VBWT. The equations are based on the formulations proposed by Bahadur [44] and Thein et al. [45].

In any spring system, the first concept to cover is Hooke's law which allows us to determine the force required to extend or compress the spring or, given the other variables, determine the spring stiffness.

$$F = Kx \quad (2)$$

where  $F$ ,  $K$ , and  $x$  are the force, spring stiffness, and the extension or compression of the spring, respectively. Furthermore, given the principle of operation of the spring is based on a mass-spring system, we need to identify the natural frequency of this system ( $f_n$ )

$$f_n = \frac{1}{2\pi} * \sqrt{\frac{k}{m}} \quad (3)$$

where  $m$  is the mass of the mast; additionally, since the proposed geometry can be described as a cantilever, given the bottom end is fixed and the upper mast is free, the deflection of the cantilever-beam relation can be described by:

$$\delta = \frac{FL^3}{3EI} \quad (4)$$

where in Equation (4),  $F$ ,  $L$ ,  $E$ , and  $I$  are the force applied, length, modulus of elasticity, and the moment of inertia of the beam cross-section, respectively. Given the mast material used in the simulation is Aluminum 2700, with a weight of 18 kg, we can begin to estimate the total force acting on each spring to be

$$F_{total} = F_{gravity} + F_{wind} \quad (5)$$

where  $F_{gravity} = 176.58$  N and  $F_{wind} = \frac{1}{2}C_d A \rho v^2 = 100.8$  N, and where  $C_d$  is the drag coefficient obtained through CFD simulations,  $A$  is the mast surface area,  $\rho$  is the density of air at room temperature ( $1.2$  kg/m<sup>3</sup>), and  $v$  is the wind speed (which in this case is 10 m/s). Thus, a total force is applied of 277.38 N. Additionally, from Equation (4), the deflection of the mast is  $\delta = 0.3$  m, and we can obtain the stiffness of each spring to be

$$K = \frac{F_{total}}{\delta} \quad (6)$$

Approximately,  $K = 925$  N/m for each spring, as shown in Figure 5



**Figure 5.** Schematic of a VBWT system with base and spring design. The above system is used for both models.

### 2.3. Simulation Model

Numerical simulation is one of the tools used to understand the behavior of the structure and the aerodynamics around it. To be able to simulate the case, two-way fluid–solid interface (FSI) was used, to enable the transfer of the solution and the data between the two models. Ansys Workbench will be used to perform the CFD and to obtain an approximation of the behavior. Using FSI requires discretizing the solid domain from the fluid domain. Transient-structural and -fluent are the two modules used to simulate the case. Two different cases were simulated, to see how modification affects vortex shedding and flow behavior. Two different mast structures were generated using Fusion 360, as shown in Figure 6. Each geometry was modeled to be hollow, with a thickness of 1 mm, since the study depends on the mass of the structure. Table 1 summarizes the dimensions of the structures proposed.

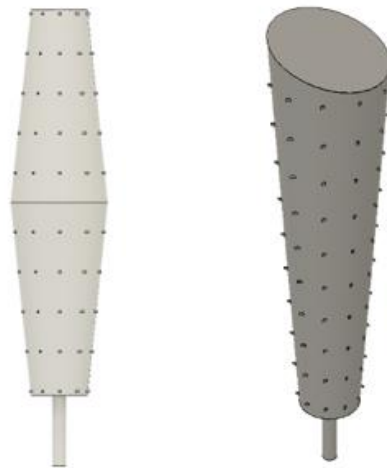


**Figure 6.** Schematic of a VBWT-system configuration used in the simulation.

**Table 1.** Dimensions of different sections in the proposed VBWT models in mm.

Part	Model 1 (mm)	Model 2 (mm)
a	760	420
b	420	420
c	100	100
d	3000	3000
e	2670	720
f	160	135
g	260	290

### 2.3.1. CFD-Simulation Set-up and Governing Equations

The design and analysis of a VBWT system heavily depend on the CFD-simulation set-up, as it allows us to predict and understand the behavior of the airflow pattern around the VBWT and to establish an understanding of the vortex shedding occurring because of the body. In this study, we used ANSYS Fluent to model the airflow around the VBWT. The governing equations of the model were the compressible Navier–Stokes (N-S) equations. These equations are transient, coupled, and non-linear, as they express the correlation between the velocity, density, and pressure of the system [46].

$$\frac{\partial \rho}{\partial t} + \frac{\partial}{\partial x_j} (\rho u_j) = 0 \quad (7)$$

$$\frac{\partial (\rho u_i)}{\partial t} + \frac{\partial (\rho u_j u_i)}{\partial x_j} = -\frac{\partial p}{\partial x_i} + \frac{\partial \sigma_{ij}}{\partial x_j} + \frac{\partial \tau_{ij}}{\partial x_j} \quad (8)$$

where  $\rho$  and  $u$  are the air density and velocity components. Additionally, in Equation (8) the RHS term  $\sigma_{ij}$  is the viscous stress tensor, defined by the following:

$$\sigma_{ij} = \mu \left[ \left( \frac{\partial u_i}{\partial x_j} + \frac{\partial u_j}{\partial x_i} - \frac{2}{3} \delta_{ij} \frac{\partial u_k}{\partial x_k} \right) \right] \quad (9)$$

Assigning the boundary conditions to any FEA problem is a critical step, which can determine the functionality and reliability of the results obtained. Thus, for this study, the following boundary conditions were introduced to the CFD analysis of the VBWT, along with the meshing scheme for the model. In this module, the solid body is suppressed, and the fluid body only is used. The boundary conditions applied to the model were a 10 m/s velocity inlet and an outlet, and the rest were selected as walls. The top and the side were selected as having a slip condition. Figure 7 shows the boundary conditions.

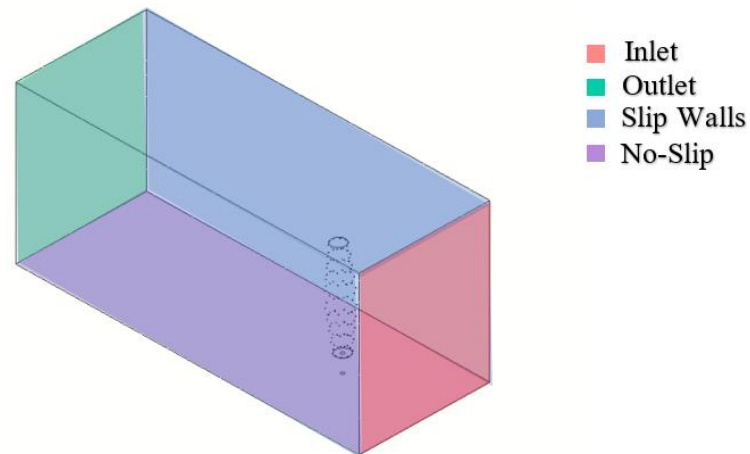


**Figure 7.** Fluent-Simulation model boundary conditions.

The next step is meshing the fluid domain. A value of  $y^+ \approx 1$  was maintained, to allow better capture of the behavior near the structure. Denser elements were applied at the vortex generators and behind the structure, to be able to capture the flow around them and the behavior at the wake region. A total number of 1,500,000 elements were defined. A detailed view of the mesh generated is illustrated in Figure 8.

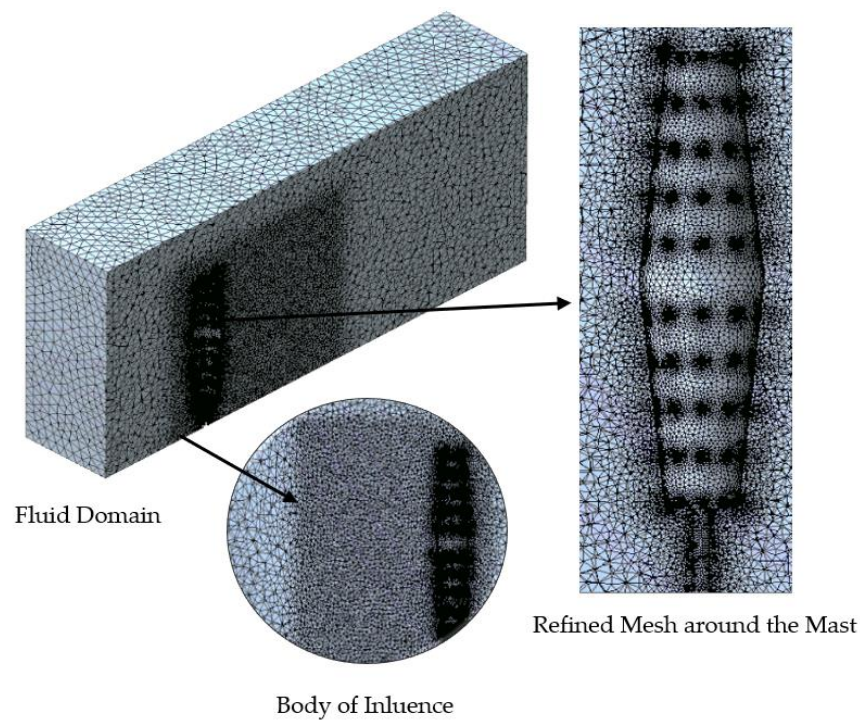


**Figure 8.** Detailed View of the Meshing Scheme generated for the CFD study.

To capture the phenomena behind the structure, the number of elements should be denser; thus, the body of influence was used to increase the element at that specific area. The gravity effect was applied on the mast at a transient condition. The  $k-\omega$  SST model was used, since it blends both the  $k-\omega$  and  $k-\epsilon$  models, which means it has the effect of capturing the effects both near the surface and away from it. The governing equations for the  $k-\omega$  SST model are obtained from the formulation by Menter [47].

$$\frac{\partial k}{\partial t} + u_i \frac{\partial k}{\partial x_j} = P_k - \beta k \omega + \frac{\partial}{\partial x_j} \left( (v + \sigma_k v_\tau) \frac{\partial k}{\partial x_j} \right) \quad (10)$$

$$\rho(V \cdot \nabla V) = -\nabla p + \mu \nabla^2 V + S \quad (11)$$

$$(\nabla \cdot \rho V) = 0 \quad (12)$$

In summary, the following parameters were used in the calculation procedure, and are summarized in Table 2.

**Table 2.** Summary of the parameters used in the simulation setup.

Parameter	Value
Time-Step Size (s)	$7.5 \times 10^{-4}$
Number of Steps	6667
Mesh Elements	1,500,000
Saving Duration	Every 15 TS
Flow Time (s)	5

### 2.3.2. Transient Structural Simulation

In this module, the fluid body is suppressed, and the solid body only is used. Aluminum was chosen to be the material of the structure, with a mass of 18 kg. The transient structural analysis employs ANSYS APDL solver, which is defined as an implicit solver, as opposed to the rigid dynamics solver, which is modeled as an explicit solver. Furthermore, the governing equation for a transient structural study takes the input loads as a function of time, and considers the inertial effects, as opposed to static studies.

$$[M] \{ \ddot{X} \}(t) + [C] \{ \dot{X} \}(t) + [K] \{ X \}(t) = \{ f \}(t) \quad (13)$$

where  $[M]$ ,  $[C]$ , and  $[K]$  are the mass, damping, and stiffness matrices of the system, respectively, which are derived using the Galerkin Method:

$$[M] = \int_V \rho N^T N dV \quad (14)$$

$$[K] = \int_V B^T D B dV \quad (15)$$

$$[C] = \int_V \mu N^T N dV \quad (16)$$

The next step is meshing the structure, which means discretizing the model into a small element, so the solver can apply the boundary condition and obtain the solution on cells. A total number of 150,000 elements were defined, as shown in Figure 9. A fixed support was applied on the bottom face of the structure, and all the faces, excluding the inner faces and the bottom face, were selected for the fluid–solid interface. This allows the transfer of the deformation, movement, or any fluent parameter. The solution was set to run for 5 s, and the time-step size was 0.00075 s.

Additionally, the following boundary conditions were defined for the structure, where a fixed support was defined at the lower part of the mast and an FSI BC was defined on the surfaces of the mast, as illustrated in Figure 10.

Finally, the interaction between both studies was modeled, through the coupling of two-way FSI simulations, as shown in Figure 11.

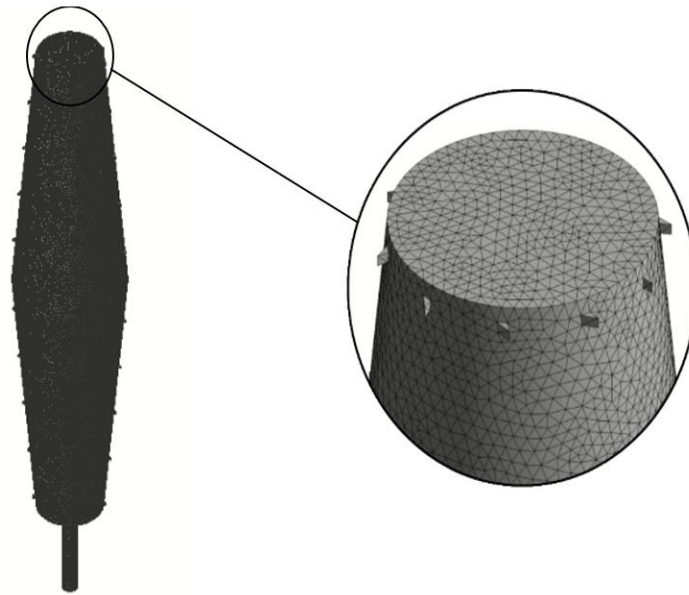


Figure 9. Detailed View of the Meshing Scheme generated for the Transient Structural study.

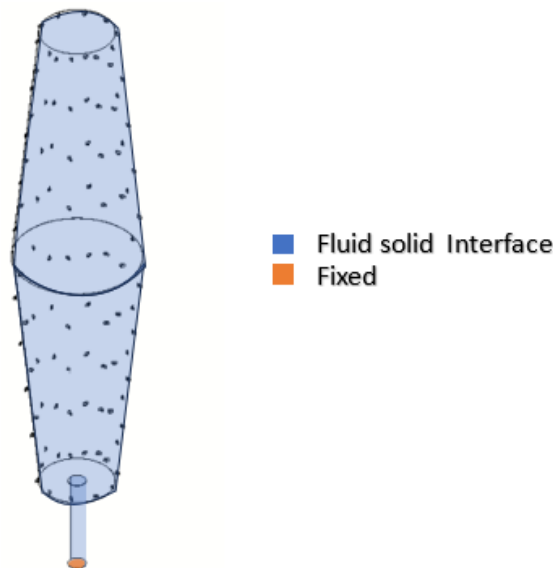


Figure 10. Boundary Conditions for the Transient Structural Study.

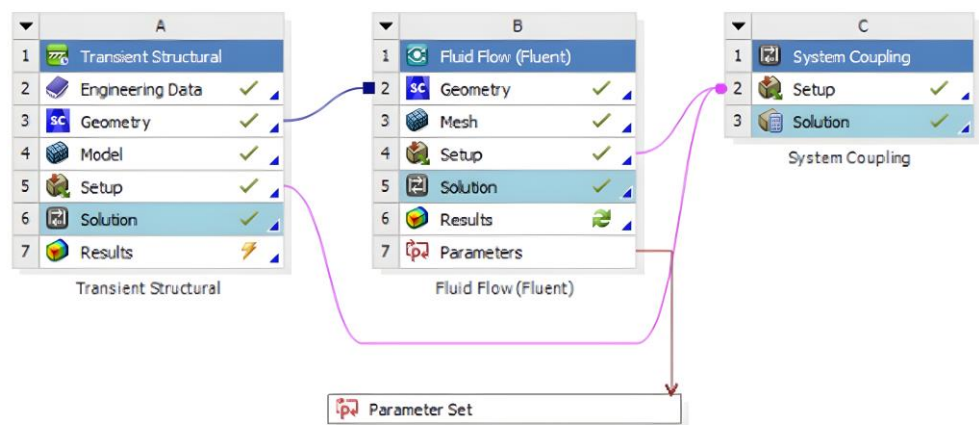
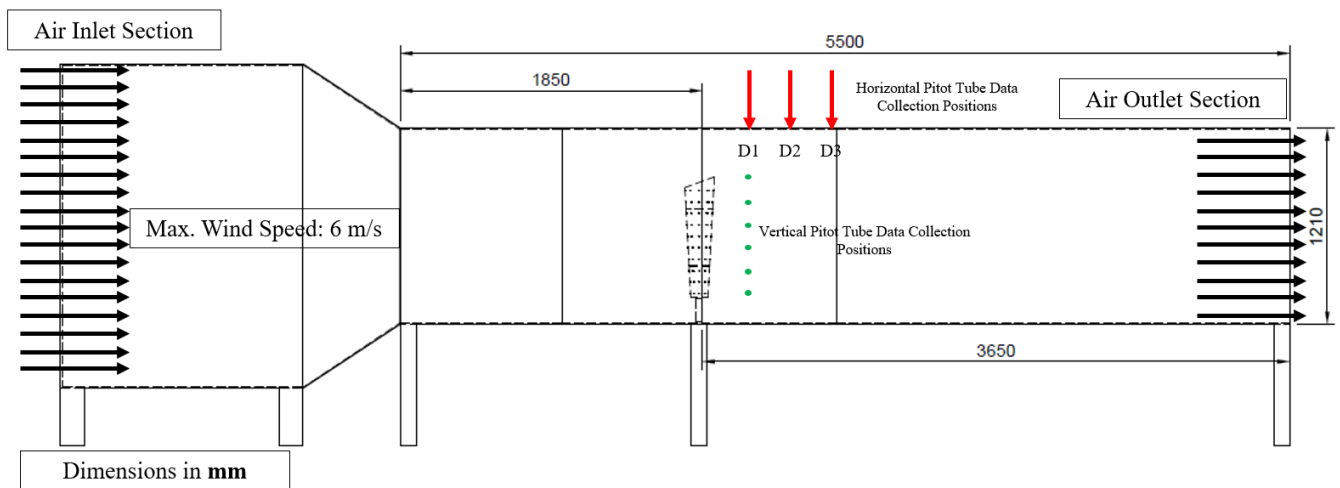


Figure 11. Final Simulation System to model Two-Way FSI simulation.

#### 2.4. Experimental Methods

Experimental work is needed to further understand the numerically obtained results and to verify them, where needed. Figure 12 shows the experimental setup plan and schematic, which sets the procedure to be followed when conducting the experimental work on the VBWT, in which a series of wind-tunnel tests will be performed to record flow-related values and structure-related values, using a set of instruments and sensors. Figure 13 shows the actual wind-tunnel research setup used in the mechanical engineering laboratory at Abu Dhabi University.



**Figure 12.** Wind-tunnel experiment setup: dimensions, sizing, placement points of the flow sensor, and maximum wind-speed flow.



**Figure 13.** A wind-tunnel-testing setup was used to perform the experimental analysis.

To obtain the data needed for further analysis, understanding, and verification of the numerical data, a set of instruments is used, including a flow velocity meter, and an ultrasonic motion sensor, shown in Figure 14. The flow velocity meter (Pitot Tube) is a digital sensor used to measure the instantaneous and average velocity of the wind flowing around the VBWT, which provides insights into the flow pattern. On the other hand, the ultrasonic motion sensor is a digital sensor that captures the displacement, velocity, and acceleration of the VBWT, over a set period, which helps capture the oscillation magnitudes and velocities.



**Figure 14.** Ultrasonic motion-detection and measuring instruments are used to measure the displacement, velocity, and acceleration of the VBWT.

### 3. Results and Discussion

In this section, the findings from two simulated systems of bladeless wind turbines are shown, at a flow time of 5 s. The main goal of these runs was to gain knowledge about the turbine structure, vibration patterns, and the associated flow phenomena, particularly in relation to its motion. The outcomes we attained provide us with an approximation of how the turbine behaves in various scenarios. Informational plots and contours that graphically represent these findings are presented in this section.

#### 3.1. Two-Way FSI Results for Model 1

The first and main case analyzed in this study was Model 1, illustrated in Figure 3. For this case, the total flow time was 5 s, and we were able to obtain valuable insights on the oscillatory behavior and flow patterns around it. Figure 15 below illustrates the velocity contours for the first third of the flow time, which is observed at 1.5 s.

During the initial stage of the flow, we begin to observe a distinctive pattern through the illustrated velocity contours. The yellow spots are observed behind the wake region of the mast, which signifies the presence of trailing vortices behind the mast as a result of the interaction between the wind flow and the VBWT mast. The small vortices behind the mast illustrate the initiation of vortex shedding. To further observe the flow directions, we plotted a vector surface over the contour, which further clarified the initiation of the shedding process. Analyzing the results at a greater flow time, i.e., 4.5 and 5 s, we were able to see a vortex-shedding pattern that can be characterized as a transition to the critical regime, where a lock-in region might be observed as the mast's natural frequency begins to sync with the vortex-shedding frequency. Hence, larger vortices can be observed, as illustrated by the contours and vector surfaces in Figure 16.

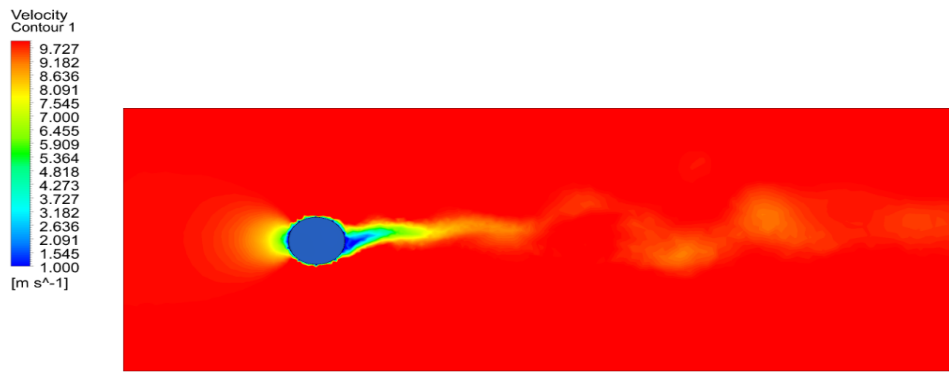


**Figure 15.** Velocity contours for Model 1 during the first 1.5 s of flow time, highlighting the growth of the vortices downstream of the fluid domain.

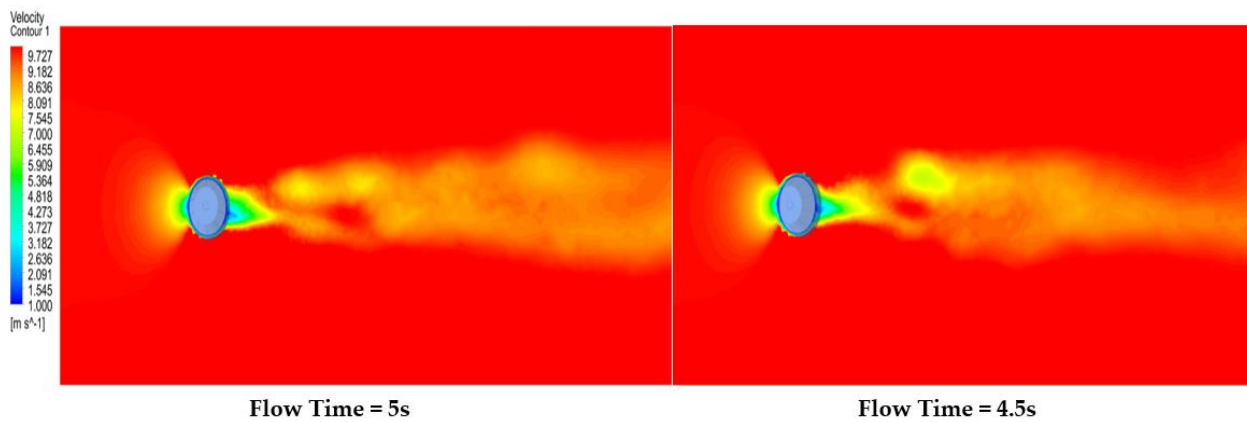


**Figure 16.** Velocity contours for Model 1 during the first 4.5 s and 5 s of flow time, highlighting the lock-in region downstream of the fluid domain.

Additionally, by plotting the 3D streamlines, we were able to observe swirling patterns behind the mast; however, they did not show very high strength, and thus we can examine further areas for optimization in the structure. On the other hand, the presence of the swirling patterns denotes the formation of vortices and vortex shedding behind the mast, which is the result we are interested in when designing VBWT. By further examining the flow behavior around the mast, we generated volume rendering using the Invariant Q criterion and the velocity-swirling strength. These methods allow us to visualize and understand the detailed vortex characteristics in the flow field, as illustrated in the volume rendering shown in Figure 17.

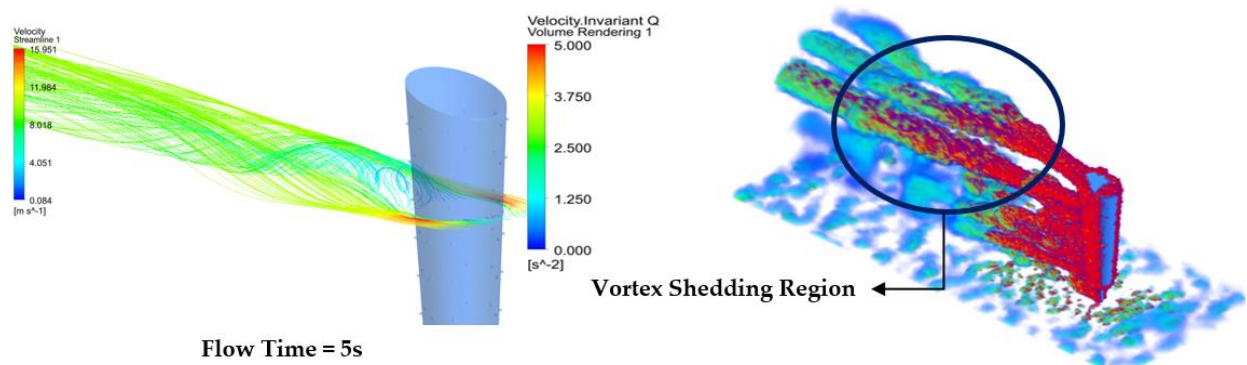


**Figure 17.** Three-dimensional velocity streamlines highlight the swirling pattern and emergence of vortices, in addition to the volume rendering, which allows us to identify where the vortices begin to shed.

To understand the dynamic behavior of the proposed VBWT model, we analyzed the velocity vs. time plots at different points behind the mast, i.e., 1.5 and 3 m horizontally. However, six points were selected at different vertical heights to visualize the oscillatory behavior at different regions, which is essential in observing temporal variations in the velocity of the air past the VBWT. This can give us insights into how the velocity changes affect the oscillatory behavior of the turbine, and reveal details about the periodicity of the vortices. The analysis points are shown and illustrated in Figure 18, below.

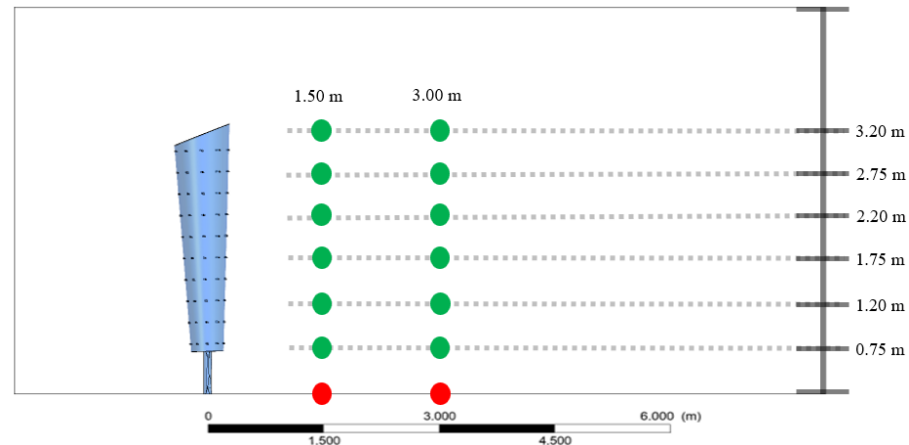


**Figure 18.** Velocity- vs. time-analysis points illustrated over the fluid domain.

Based on the observations in Figure 19 for the velocity vs. time plots, we can draw the following conclusions:

1. At points closer to the ground, higher amplitudes are observed in the velocity profile. This can be attributed to the higher vortex shedding, due to proximity to the ground. Thus, the behavior of the flow can be more chaotic and turbulent.
2. Furthermore, we can relate the above behavior to the wind profile. Going back to classical fluid mechanics, at higher elevations, the wind is generally faster and more consistent. Therefore, less turbulence is observed in the velocity profile for the first three points.
3. As described by the structure of the mast, there are more vibrations at the base, which decrease the waves propagated towards the top of the mast. Hence, there is lower vortex shedding at the top.

Furthermore, we were able to observe the highest concentration of magnitudes between 0 and 5 Hz in the FFT analysis of the coefficient of lift, shown in Figure 20. This can be described by the high energy concentration and oscillatory behavior generated between these frequencies. The notable concentration of magnitudes between 0 and 5 Hz in the FFT analysis of the coefficient of lift unveils a crucial frequency range, wherein the turbine demonstrates heightened vibrational energy concentration and oscillatory activity. The oscillatory behavior within this frequency ambit is reflective of the intrinsic resonance phenomena of the VBWT, which is pivotal to its energy-harvesting capability. The resonance conditions, engendered by the interaction between the airstream and the turbine structure, could potentially give rise to augmented lift forces, thereby amplifying the turbine's capacity to harvest energy from wind. Furthermore, comprehending the frequency-domain behavior of the coefficient of lift lays a substantial groundwork for refining the turbine's design and operational parameters. By meticulously adjusting these parameters to effectively leverage the identified resonance behavior, there emerges a promising pathway to bolster the VBWT's energy-generation efficiency. This discernment also expands the horizon for delving into inventive design alterations or control strategies poised to capitalize on the identified frequency-dependent dynamics, thereby further augmenting the VBWT's renewable-energy-generation potential.

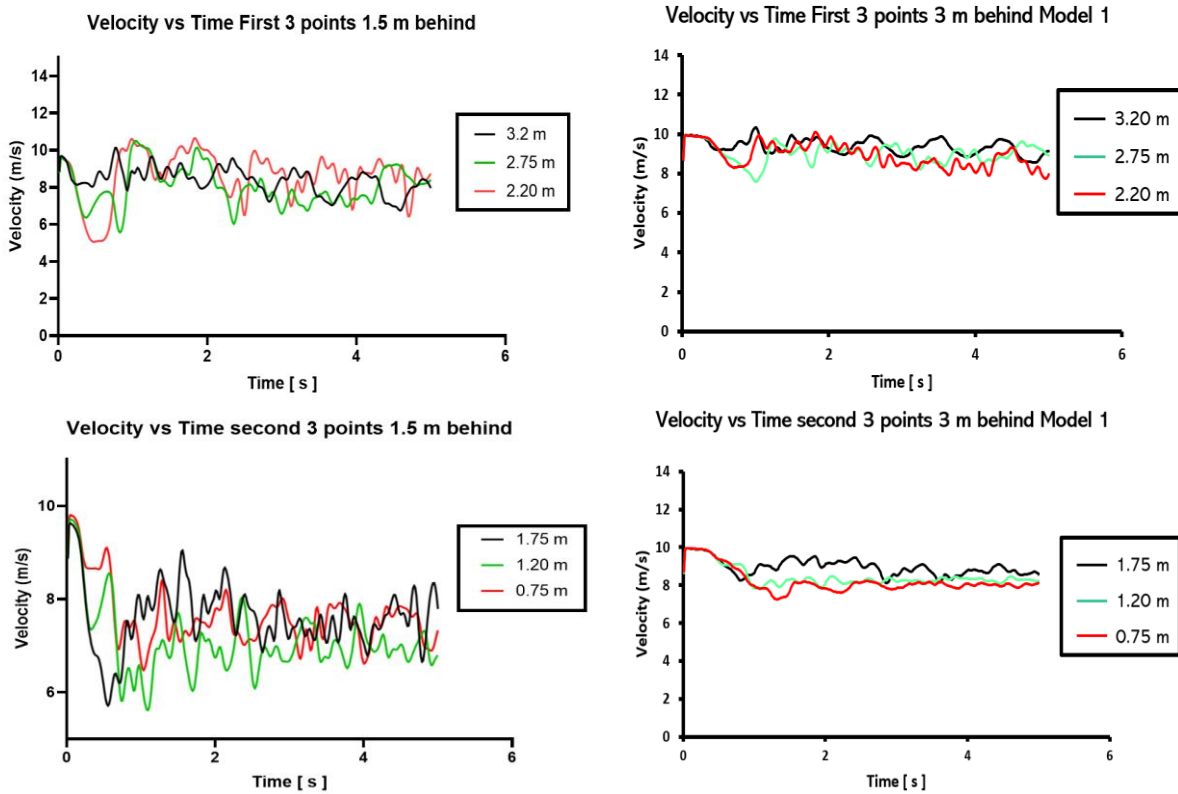


Figure 19. Velocity vs. time plots at varying vertical locations 1.5 and 3 m behind the mast of the VBWT.

### FFT $C_L$

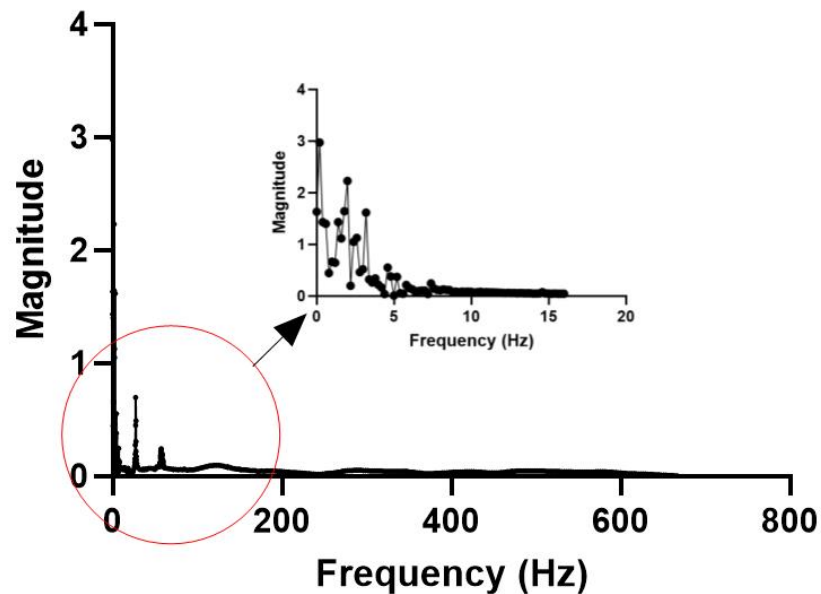
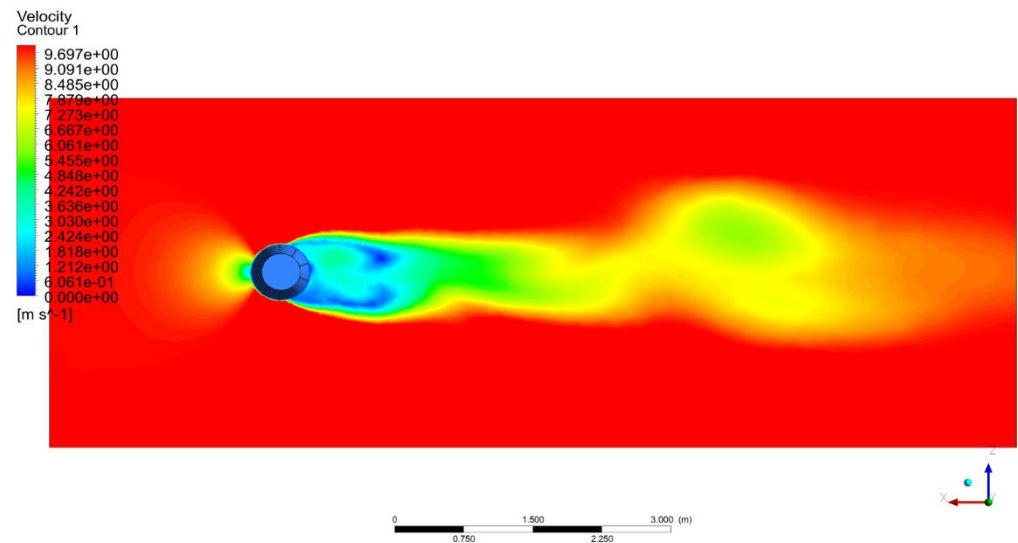


Figure 20. FFT transform of the Coefficient of Lift  $C_L$  from the time to the frequency domain.

#### 3.2. Two-Way FSI Results for Model 2

Model 2, which is seen in Figure 3, was the second case examined in this investigation. In this instance, the overall flow time was five seconds, and within that time we were able to learn important things about the oscillatory behavior and the flow patterns surrounding it. The velocity contours during the first third of the flow duration, which is recorded at 1.5 s, are shown in Figure 21, below.



**Figure 21.** Velocity contours over Model 2 during the first 1.5 s of flow time highlighting the growth of the vortices downstream of the fluid domain initiated at the wake region.

Analyzing this model, we were able to observe clearer vorticity at the initial stages of the flow, i.e., 1.5 s. Furthermore, the velocity contour presents a clearer initiation of the Von Karman Vortex Street phenomenon, which allows us to assume that this model induces higher vortex shedding due to its converging diverging structure. The appearance of the vorticity at an early stage in the flow can suggest that this design might begin to harvest energy quicker than the previous model after the onset of the wind flow. Furthermore, based on the velocity contour observed in Figure 21, we can showcase a prominent inception of the Karman Vortex Street phenomenon. This is described as a pattern of swirling vortices. Moreover, the fact that the vortex street flow pattern is observed at an early stage suggests that the model is successfully causing unsteady separation of the flow, and inducing vortex shedding. This can be extremely beneficial in generating energy from this model, and can be efficient, as vortex shedding occurs at the earliest onset of flow. Additionally, at increased flow time we can observe higher vortex shedding and a stronger illustration of the Von Karman Vortex Street phenomenon. Figure 22 highlights the vortex shedding at flow times of 4.5 and 5 s.

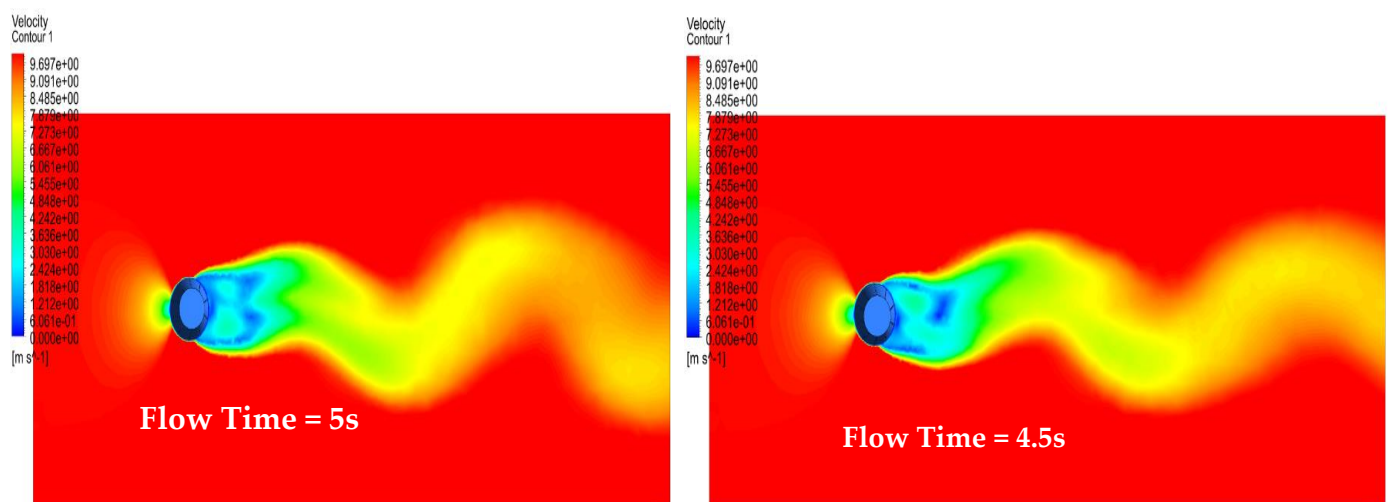


**Figure 22.** Velocity contours for Model 2 during 4.5 s and 5 s of flow time, highlighting the lock-in region downstream of the fluid domain and the Von Karman Vortex Street flow pattern.

To further understand the dominance of vortex shedding and swirling strength in the flow field of the model, we were able to generate the following volume renderings to highlight the vortex-shedding phenomenon in Figure 22. Furthermore, we can attribute the stronger swirling and vorticity in this model to the converging–diverging design of the mast. It can be assumed that the shape may promote more pronounced areas of pressure difference around the mast flow field. Thus, geometry begins to cause the velocity of the incoming wind to constantly increase and decrease, hence promoting a higher-pressure change, which is a critical factor in initiating vortex-shedding patterns. However, it is important to analyze the structural influence of these strong vortices on the mast integrity.

Moreover, we plotted the 3D streamlines along the flow field of the second VBWT model. After analyzing the streamlines illustrated in Figure 23, we were able to identify a large vortex in the wake of the mast. This can indicate the presence of either a series of shed vortices or a single-like vortex. We can conclude that this geometry presents much more initiation of vortex shedding and can generate more power as a renewable energy source.

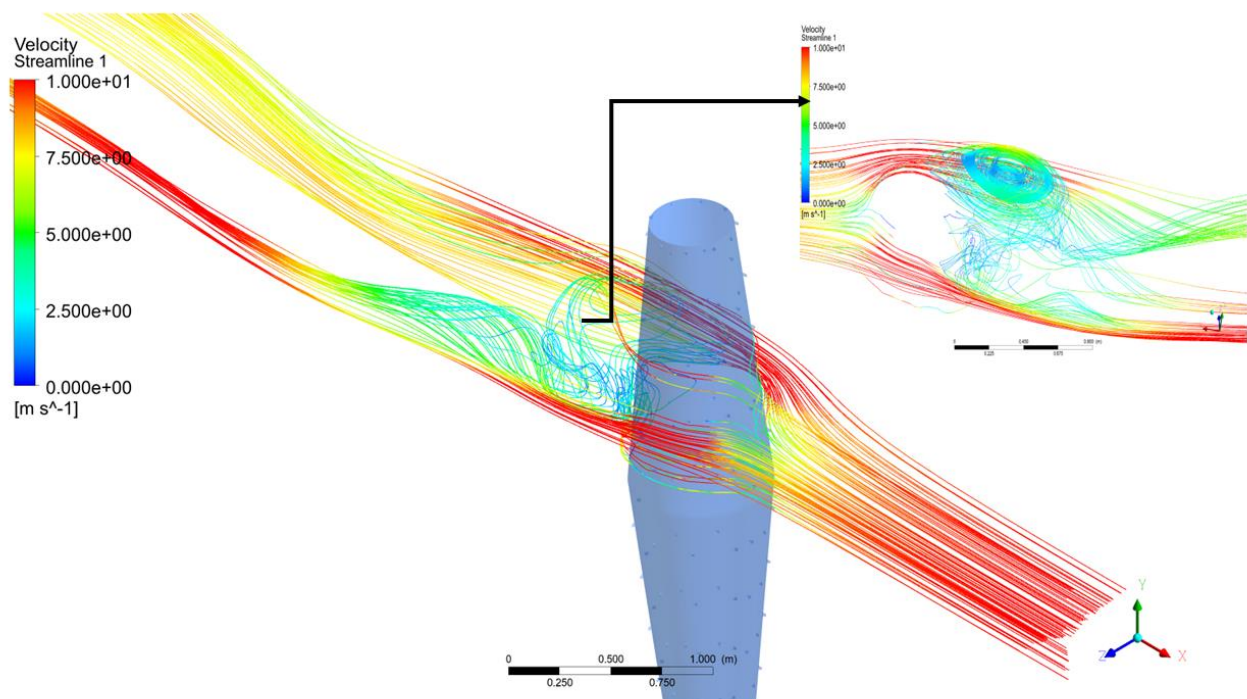


**Figure 23.** Three-dimensional velocity streamlines highlighting vortex formation in the wake region of the model.

We repeated the procedures used for the first model to comprehend the dynamic behavior of the suggested VBWT model. This involved creating velocity vs. time charts at 1.5 and 3 m horizontal distances behind the mast, depicted in Figure 24. To show the oscillatory behavior at various areas, however, six points at various vertical heights were chosen. This is crucial for analyzing temporal fluctuations in air velocity past the VBWT. This can help us understand how velocity changes impact the turbine’s oscillatory behavior and elucidate the periodicity of the vortices.

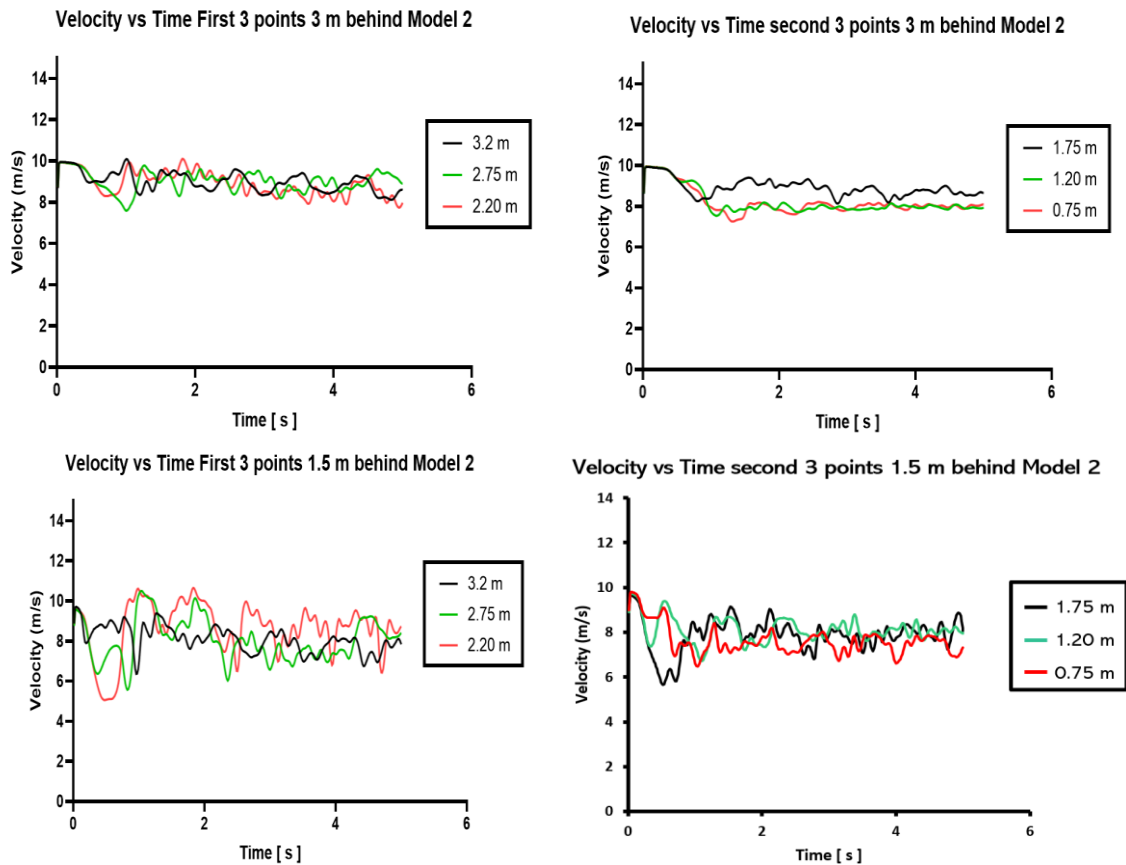


**Figure 24.** Velocity vs. time plots at varying vertical locations 1.5 and 3 m behind the mast of the VBWT, from Model 2.

Based on the observations above for the velocity vs. time plots, we can deduce the following conclusions. The decrease in the velocity amplitudes at further points away from the mast can be attributed to the energy-dissipation mechanism of the VBWT model as it moves away from the mast.

1. At a closer distance, i.e., 1.5 m, the flow is strongly influenced by the vortex shedding occurring downstream of the VBWT, thus causing a larger fluctuation in the velocity, which translates to the higher amplitudes observed in the above plots.
2. At a further distance, i.e., 3 m, the fluctuations begin to dampen, because the energy from the shedding begins to dissipate as it mixes with the surrounding airflow and environmental conditions, such as the pressure.

Furthermore, we were able to observe the highest concentration of magnitudes between 0 and 9 Hz in the FFT analysis of the coefficient of lift, as evident in Figure 25. This can be described by the high energy concentration and oscillatory behavior generated between these frequencies. However, compared to the first model, this model had higher magnitudes at similar frequencies. This can be attributed to the structural changes, which could have impacted the lift forces, leading to a change in the magnitude. Additionally, the higher vorticity generated by this model can signal reduced damping; this reduced damping can lead to higher peak amplitudes at resonance frequencies, as observed in the enlarged section of the FFT plot.

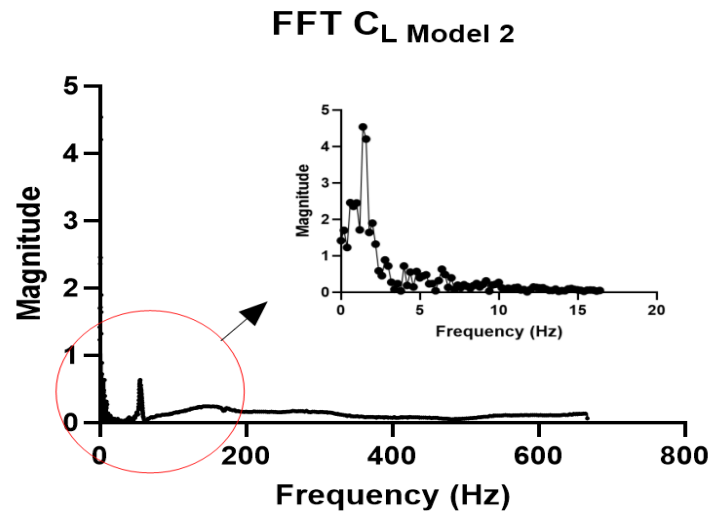


Figure 25. FFT transform of the Coefficient of Lift  $C_L$  from the time to the frequency domain for Model 2.

### 3.3. Power Calculation

The power calculation process is carried out for both the experimental and simulation data. The formulation for the power analysis is highly non-linear, due to the changes in the flow conditions, which in turn vary the forces applied on the wind turbine (lift, drag, vibration, etc.). To simplify matters, we apply a linear form for the power evaluation, since the forces are not entirely measured experimentally, and the equation is summed below.

$$P_{out} = F_{wind} \cdot (v_{mast}) \quad (17)$$

where  $P_{out}$  is the linear approximated form of the power output of the VBWT,  $F_{wind}$  is the directly applied force by the wind on the mast surface facing the inlet, and  $v_{mast}$  is the velocity of the mast, averaged over time. The force applied is shown below.

$$F_{wind} = P_{app} * (A_s) \quad (18)$$

where  $P_{app}$  is the applied wind pressure on the mast surface, and  $A_s$  is the surface area of the mast. The applied wind pressure is found through the equation below.

$$P_{app} = 0.5 * \rho_{wind} * (v_{flow})^2 @ \text{Room Condition} \quad (19)$$

The power is then found as follows, for the simulation analysis. Flow velocity is noted to be 10 m/s, air density at room condition is approximately 1.204 kg/m<sup>3</sup> according to the International Standard Atmosphere (ISA), and thus,  $P_{app}$  is found to be 60.2 Pa.

The surface area of the mast is 5.0255 m<sup>2</sup> for the full-scale model, which was simulated, and thus  $F_{wind}$  comes out to be 302.5351 N. The velocity of the mast is recorded in the simulation as a time series for 5 s; we use this to obtain the power with respect to time. So,  $P_{out}$  comes out to be as shown in Figure 26 below, which is found using element-wise multiplication of the force with the mast velocity, and is carried out using a simple MATLAB script to make the process efficient.

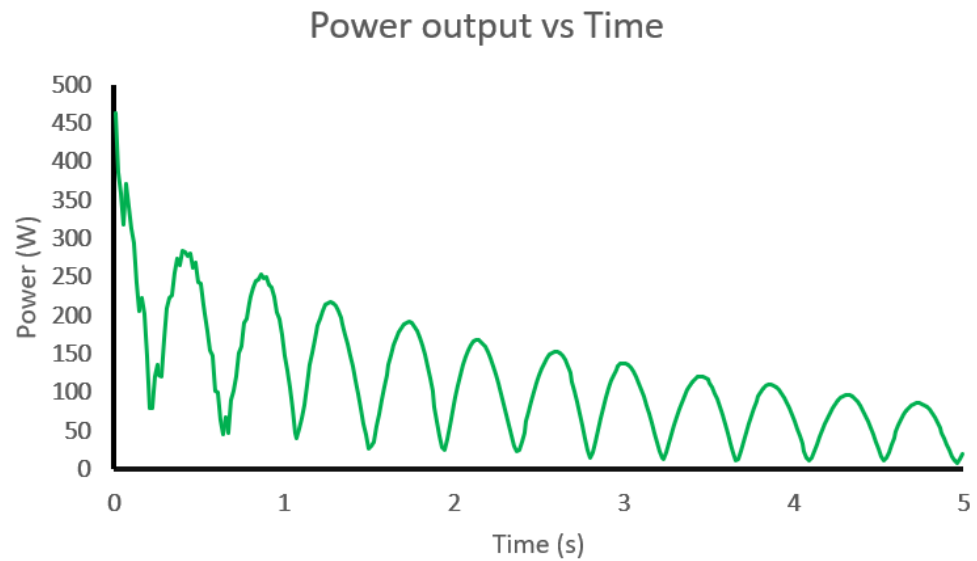


**Figure 26.** Output Power of the VBWT through the simulation data, for 5 s.

For the experimental data, the model is scaled down to 25% for appropriate wind-tunnel fitment, the surface area is found to be  $0.3241974 \text{ m}^2$ , and the wind-flow velocity is  $6 \text{ m/s}$ ; thus, the wind pressure is  $21.672 \text{ Pa}$ , and the corresponding force is  $7.026 \text{ N}$ , and thus the power output is shown in Figure 27, below. The noisy behavior in the figure can be attributed to disturbances and imperfections in the flow behavior inside the wind tunnel. Additionally, the power output can be increased by simply using an array of multiple bladeless wind turbines.

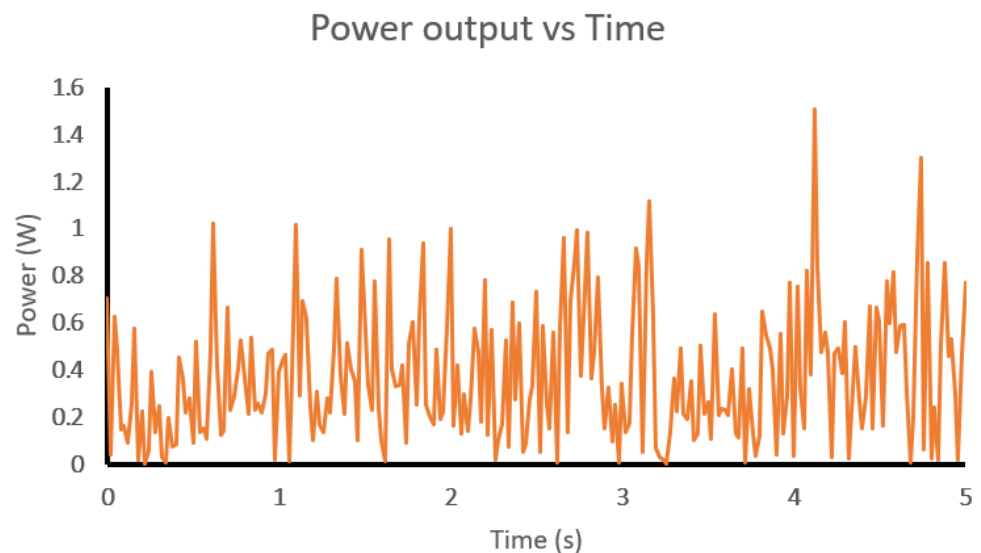


**Figure 27.** Output Power of the VBWT from the experimental data, for 5 s.

### 3.4. Experimental Results

Experimental work was carried out to correlate the simulation results obtained with actual physical results. This is illustrated in Figure 12 in Section 2.4, in which the VBWT is shown placed  $1850 \text{ mm}$  after the converging duct of the wind tunnel. This is also shown in Figure 28, which illustrates the actual experimental condition. After placing the VBWT as mentioned, different readings were recorded using two distinct sensors; one is a pitot-tube flow-speed sensor, and the other is an ultrasonic motion sensor. The pitot-tube recordings were taken at different horizontal and vertical positions, to roughly capture the flow pattern behind the mast; these points are shown and illustrated in Figure 12, as well, where the

horizontal points are taken as mast diameters ( $D_1 = 10.7\text{ cm}$ ,  $D_2 = 21.4\text{ cm}$ ,  $D_3 = 32.1\text{ cm}$ ) and the vertical points are taken along the length of the mast (30 cm to 90 cm). However, for the ultrasonic motion sensor, the most appropriate position is to be behind the mast, with a rough spacing of 1. The pitot-tube readings and ultrasonic-motion-sensor readings are shown in Figures 29–31, respectively.



Figure 28. VBWT placement in the wind tunnel and the wind-flow-sensor attachment.

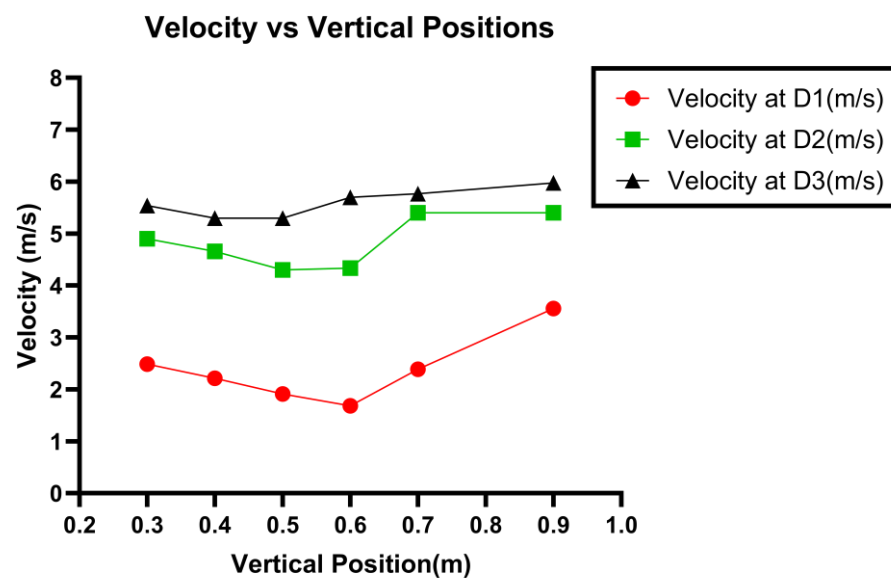


Figure 29. Pitot-tube flow-velocity readings against the vertical positions.

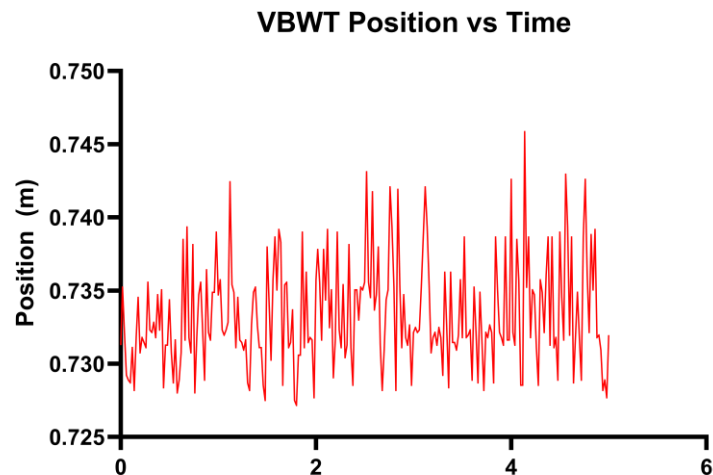


Figure 30. Motion sensor data, VBWT position vs. time.

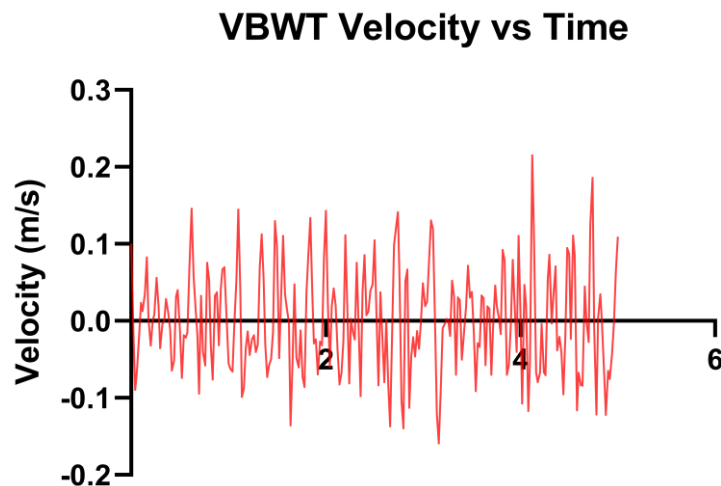


Figure 31. Motion sensor data, VBWT velocity vs. time.

As previously mentioned, the pitot-tube readings were recorded to evaluate the flow conditions behind the mast. To understand Figure 29, we first need to look back at Figure 12, to have both the horizontal and vertical points as a reference. At vertical position 0.3 m, the velocity should be relatively higher, due to the smaller mast section at that height point, while maintaining a lower value, due to being close to the mast (at  $D_1$ ). We then notice a decrease in the velocity value as we go up in the vertical positions, until we reach the tip of the mast, which shows a higher velocity than the other points. This pattern is noticed in the other horizontal positions ( $D_2$ , and  $D_3$ ). It would be logical for the average velocity at  $D_2$  to be lower than  $D_3$  and higher than  $D_1$ ; however, some irregularity in the flow is noticed in the graph at this horizontal position, which could indicate the presence of turbulent vortices. For the motion-sensor readings, we begin with Figure 30, which shows the change in the mast position over time, in which we note that the mast roughly (on average) deflects 15 m, disregarding the irregularity of the motion occurring due to disturbances in the flow. And for Figure 31, we notice that the VBWT moves, on average, at a speed of 0.15 m/s. With the flow speed being 6 m/s, the smaller deflection and mast-motion-velocity values are related to the stiffness of the springs and the overall design, and in such systems, lower velocities and deflections are favored, due to the resulting increase in the frequency of the motion, which correlates to a higher overall power output.

### 3.5. Energy Storage Systems

There are various technologies and energy storage mechanisms present in the literature [48–51], each having its strengths and weaknesses; however, since the goal of the proposed system is to present a compact RES, the selection of an energy storage system needs to be considering two factors: complexity and efficiency. There are four main categories of energy storage systems: mechanical, electrochemical, electrical, and hybrid energy storage systems. Mechanical energy storage systems such as Pumped Hydroelectric Energy Storage (PHES) are very efficient, as they store excess energy by pumped water as gravitational potential energy, which makes them very efficient when the renewable energy generation is low [49]. However, such systems require a large geographical footprint and can be very costly and complex to set up. On the other hand, Electrical Energy Storage Systems (EES), such as supercapacitors, offer fast charge and discharge rates but have a low energy density, and thus their applicability for long-term energy storage becomes very limited [52]. Hybrid systems can usually combine mechanical and electrochemical systems, which offer significant versatility but often require a high cost. Therefore, the remaining option is the Electrochemical Energy Storage System. These systems are divided into two categories: battery energy storage and fuel cells for hydrogen storage. Hydrogen energy storage systems can be very efficient, as the energy can be stored for a long time and can be produced using RES. However, this comes with several limitations, such as the need for infrastructure such as pipelines and fuel cells.

Therefore, the most suitable system is Battery Energy Storage Systems; specifically, lithium-ion batteries, considering their high efficiency and high energy density. The high energy density associated with lithium-ion batteries allows for substantial energy storage in a compact form factor. Their long cycle life ensures longevity, which maximizes the utility of stored energy from the VBWT. Moreover, the modular nature of lithium-ion batteries makes them easy to incorporate into existing setups, reducing the complexity of the overall system. Additionally, Table 3 shows how lithium-ion batteries compare to different battery chemistries in terms of cost, power, energy, and efficiency [53].

**Table 3.** Specifications of most common batteries.

Battery Chemistry	Cost	Specific Power (W/kg)	Specific Energy (Wh/kg)	Efficiency (%)
Lithium-ion	High	150–315	75–250	95–98
Lead-acid	Low	75–300	30–50	70–80
Sodium–Sulfur	High	150–20	150–240	80–90
Vanadium Redox	High	100–166	10–35	65–85
Nickel–Cadmium	Moderate	150–300	70–75	70–80
Nickel–Metal Hydride	Moderate	200–300	70–100	60–70

Battery sizing is an important step in designing a fully functional RES; this ensures that the system can efficiently store and utilize excess energy generated by the VBWT and provide reliable power during low-energy production periods. The two main factors to consider in battery sizing are the required battery capacity  $Q_{batt}$  and the number of batteries  $N_{batt}$ . These parameters are governed by several factors, such as the battery voltage, depth of discharge, days of autonomy, and the efficiency of the selected battery. The battery capacity can be calculated using Equation (20) [54]:

$$Q_{batt} = \frac{31(E_{system}) \cdot X}{V_{batt} \cdot DoD \cdot X \cdot \eta} \quad (20)$$

where  $E_{system}$ ,  $V_{batt}$ ,  $DoD$ ,  $X$ , and  $\eta$  are the system's monthly load energy, the battery nominal voltage, depth of discharge, days of autonomy (no. days a battery can sustain after

being charged by the system), and battery efficiency, respectively. Similarly, by obtaining the required battery capacity, the number of batteries can be calculated, using Equation (21).

$$N_{batt} = ENT \left( \frac{Q_{batt,min}}{Q_{batt,unit}} \right) \quad (21)$$

### 3.6. Power-Generator Conceptual Design

To generate electric power through the mechanical motion of the bladeless wind turbine, it is possible to use simple electromagnetic induction to produce an alternating electric current that could be rectified to be of a direct type. This process is reliable and simple; however, it can be further enhanced by using magnetostrictive power generation.

Magnetostrictive power generation harnesses mechanical vibrations, transforming them into electrical energy through the distinctive properties of magnetostrictive materials, which alter their magnetic characteristics under mechanical influence [55]. A prevalent design embodies a parallel-beam architecture, encompassing a rod crafted from an iron-gallium alloy, encircled by a coil, and accompanied by a permanent magnet, setting the stage for electromagnetic induction to occur [56]. The ensuing shift in the magnetic domain within the magnetostrictive material incites an electromotive force within the adjacent coil, driving electric current and thereby translating mechanical energy into an electrical form. This innovative energy-conversion avenue finds its utility in various domains, epitomizing a promising pathway for powering battery-free IoT devices and monitoring systems, broadening the horizon for self-sustained, low-power applications in modern infrastructures [57]. The concept design is rendered in Figure 32, showing a device that uses both the distinct features of a magnetostrictive power generator and a traditional induction-based power generator.

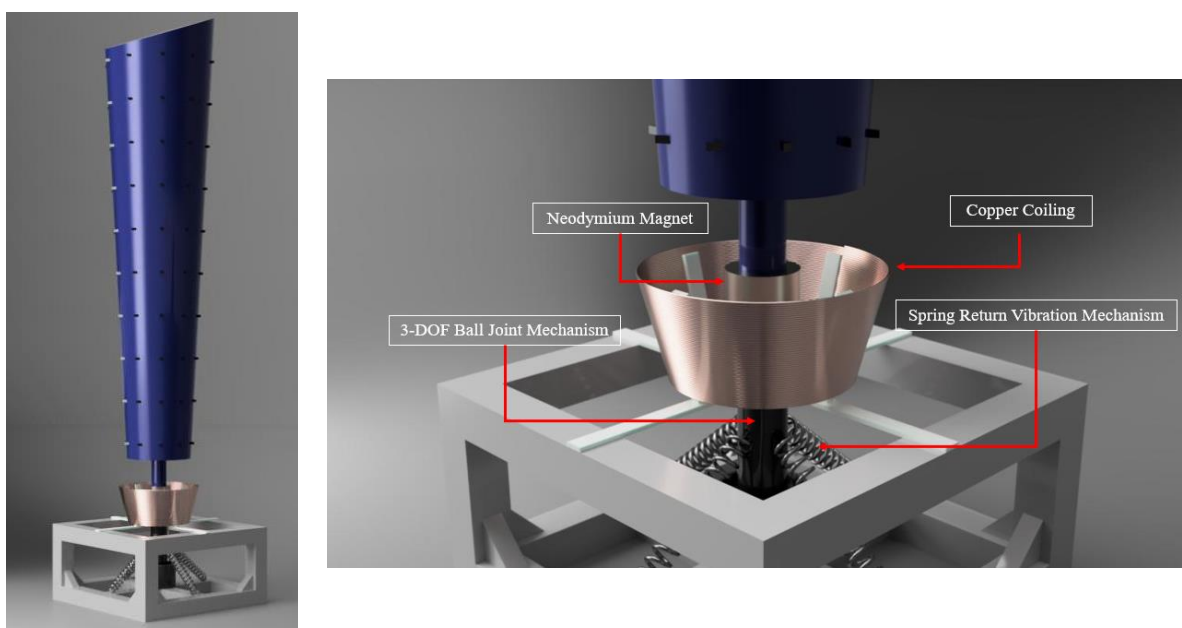


**Figure 32.** Illustration of the power-generation-system concept integrated into the Vortex Bladeless Wind Turbine.

### 3.7. Business Model and Commercialization

To commercialize the VBWT system, a business model should be developed first and foremost; this ideation process requires the use of a traditional nine-panel business model canvas. This was carried out, and is shown in Figure 33.

<p><b>Key Partners</b></p> <ol style="list-style-type: none"> <li>1. Wind turbine manufacturers for collaboration and production.</li> <li>2. Renewable energy organizations and research institutions for knowledge sharing and support.</li> <li>3. Engineering and construction firms for installation and maintenance services.</li> <li>4. Electricity grid operators for integration and distribution of generated power.</li> <li>5. Regulatory authorities for compliance with energy and environmental regulations.</li> </ol>	<p><b>Key Activities</b></p> <ol style="list-style-type: none"> <li>1. Research and development of Vortex Bladeless Wind Turbine technology.</li> <li>2. Manufacturing and assembly of Vortex Bladeless Wind Turbines.</li> <li>3. Installation and maintenance of the turbines.</li> <li>4. Marketing and promotion of the technology to potential customers.</li> <li>5. Collaboration with partners for joint projects and initiatives.</li> <li>6. Continuous innovation and improvement of the technology.</li> </ol>	<p><b>Value Propositions</b></p> <ol style="list-style-type: none"> <li>1. Environmentally friendly and aesthetically pleasing wind energy solution.</li> <li>2. Lower maintenance costs compared to traditional wind turbines.</li> <li>3. Noiseless and vibration-free operation, making it suitable for urban and residential areas.</li> <li>4. Potential for <b>integration</b> with existing renewable energy infrastructure.</li> <li>5. Scalability and adaptability to various wind conditions.</li> </ol>	<p><b>Customer Relationships</b></p> <ol style="list-style-type: none"> <li>1. Consultative approach to understand customer needs and propose tailored solutions.</li> <li>2. Timely installation and commissioning of the Vortex Bladeless Wind Turbines.</li> <li>3. Ongoing customer support and maintenance services.</li> <li>4. Regular communication and updates on new developments and improvements.</li> </ol>	<p><b>Customer Segments</b></p> <ol style="list-style-type: none"> <li>1. Energy companies and utilities looking to diversify their renewable energy portfolio.</li> <li>2. Government entities and municipalities aiming to promote clean energy solutions.</li> <li>3. Industrial and commercial businesses seeking sustainable energy alternatives.</li> <li>4. Real estate developers interested in incorporating renewable energy into their projects.</li> <li>5. Environmentally conscious consumers and communities.</li> </ol>
<p><b>Cost Structure</b></p> <ol style="list-style-type: none"> <li>1. Research and development costs for continuous innovation and improvement.</li> <li>2. Manufacturing and production expenses.</li> <li>3. Marketing and promotional activities.</li> <li>4. Installation, maintenance, and servicing costs.</li> <li>5. Compliance and regulatory expenses.</li> <li>6. Administrative and operational costs.</li> </ol>		<p><b>Revenue Streams</b></p> <ol style="list-style-type: none"> <li>1. Sales revenue from the Vortex Bladeless Wind Turbine units.</li> <li>2. Installation and maintenance services for the turbines.</li> <li>3. Licensing agreements for the use of the technology.</li> <li>4. Research and development grants and partnerships.</li> <li>5. Joint ventures and collaborations with other renewable energy companies.</li> </ol>		

Figure 33. Business model canvas.

#### 4. Conclusions

This study examined the vibration patterns, flow phenomena, and power-generation capabilities of a bladeless wind turbine over three simulation runs. The results of this study offer insightful knowledge of the operation and behavior of bladeless wind turbines. To prevent excessive vibrations that would affect the structure of the turbine, the analysis of vibration patterns showed how important it is to consider natural frequencies and modes of vibration. Bladeless wind turbines can operate more safely and effectively if vibration amplitudes and frequencies are understood and managed. The study of flow phenomena, especially vortex shedding, provided insight into the forces and interactions between the surrounding airflow and the turbine, which are caused by aerodynamics. To optimize aerodynamic performance and wind-energy extraction, design improvement can be guided by the observation of vortex-shedding frequencies. The comparison of various turbine models demonstrated the influence of design decisions on power production. Model 2 was better than Model 1 in terms of aerodynamic performance, as evidenced by increased vortex-shedding frequency and power-generation approximations. Overall, this work offers insights for future research and optimization, as well as a better knowledge of the dynamics of bladeless wind turbines. The design and operation of bladeless wind turbines highlight how important it is to take vibration properties, flow interactions, and power-generation capacities into account. Future research should investigate more variables, practical testing, and optimization methods to improve the efficiency and viability of bladeless wind turbines as a sustainable energy source.

**Author Contributions:** Conceptualization, S.S.D.; methodology, S.S.D., A.H.G. and A.B.A.T.; validation, H.H.; formal analysis, S.S.D., H.H., A.H.G., A.B.A.T. and A.A.R.; investigation, H.H., A.H.G., A.B.A.T., A.A.R. and H.F.T.; resources, S.S.D.; writing—original draft preparation, H.H., A.H.G., A.B.A.T. and H.F.T.; writing—review and editing, S.S.D., M.A. and R.A.; supervision, S.S.D., M.A. and R.A.; project administration, S.S.D.; funding acquisition, S.S.D. All authors have read and agreed to the published version of the manuscript.

**Funding:** This research was conducted at Abu Dhabi University (ADU) and funded by the Office of Research and Sponsored Programs (ORSP) at ADU [Grant number: 19300809]. And the APC was funded by both ORSP and College of Engineering at ADU. The authors gratefully acknowledge the financial support provided by Abu Dhabi University for this research project.

**Data Availability Statement:** The data presented in this study are available on request from the corresponding author. The data are not publicly available due to confidentiality concerns.

**Conflicts of Interest:** The authors declare no conflicts of interest.

## References

1. Momete, D.C. Analysis of the Potential of Clean Energy Deployment in the European Union. *IEEE Access* **2018**, *6*, 54811–54822. [[CrossRef](#)]
2. Borovik, M.R.; Albers, J.D. Participation in the Illinois Solar Renewable Energy Market. *Electr. J.* **2018**, *31*, 33–39. [[CrossRef](#)]
3. Jaszczur, M.; Hassan, Q.; Palej, P.; Abdulateef, J. Multi-Objective Optimisation of a Micro-Grid Hybrid Power System for Household Application. *Energy* **2020**, *202*, 117738. [[CrossRef](#)]
4. Hassan, Q.; Al-Hitmi, M.; Tabar, V.S.; Sameen, A.Z.; Salman, H.M.; Jaszczur, M. Middle East Energy Consumption and Potential Renewable Sources: An Overview. *Clean. Eng. Technol.* **2023**, *12*, 100599. [[CrossRef](#)]
5. Sayed, E.T.; Olabi, A.G.; Elsaid, K.; Al Radi, M.; Alqadi, R.; Ali Abdelkareem, M. Recent Progress in Renewable Energy Based-Desalination in the Middle East and North Africa MENA Region. *J. Adv. Res.* **2023**, *48*, 125–156. [[CrossRef](#)]
6. Ashfaq, A.; Ianakiev, A. Features of Fully Integrated Renewable Energy Atlas for Pakistan; Wind, Solar and Cooling. *Renew. Sustain. Energy Rev.* **2018**, *97*, 14–27. [[CrossRef](#)]
7. Qazi, A.; Hussain, F.; Rahim, N.A.B.D.; Hardaker, G.; Alghazzawi, D.; Shaban, K.; Haruna, K. Towards Sustainable Energy: A Systematic Review of Renewable Energy Sources, Technologies, and Public Opinions. *IEEE Access* **2019**, *7*, 63837–63851. [[CrossRef](#)]
8. Jaszczur, M.; Hassan, Q.; Al-Anbagi, H.N.; Palej, P. A Numerical Analysis of a HYBRID PV+WT Power System. In Proceedings of the E3S Web of Conferences, Rome, Italy, 3–6 September 2019; Volume 128.
9. Abbas, M.K.; Hassan, Q.; Jaszczur, M.; Al-Sagar, Z.S.; Hussain, A.N.; Hasan, A.; Mohamad, A. Energy Visibility of a Modeled Photovoltaic/Diesel Generator Set Connected to the Grid. *Energy Harvest. Syst.* **2022**, *9*, 27–38. [[CrossRef](#)]
10. Hassan, Q. Optimisation of Solar-Hydrogen Power System for Household Applications. *Int. J. Hydrog. Energy* **2020**, *45*, 33111–33127. [[CrossRef](#)]
11. Dall-Orsoletta, A.; Ferreira, P.; Gilson Dranka, G. Low-Carbon Technologies and Just Energy Transition: Prospects for Electric Vehicles. *Energy Convers. Manag. X* **2022**, *16*, 100271. [[CrossRef](#)]
12. Al-falahi, M.D.A.; Jayasinghe, S.D.G.; Enshaei, H. A Review on Recent Size Optimization Methodologies for Standalone Solar and Wind Hybrid Renewable Energy System. *Energy Convers. Manag.* **2017**, *143*, 252–274. [[CrossRef](#)]
13. Pervaiz, S.S.; Dol, S.S.; Alhassani, A.K.; Abdallfah, M.T.; Fares, M. Numerical Modelling and Performance Optimization of a Vertical Axis Wind Turbine. In *Energy and Environment in the Tropics*; Sulaiman, S.A., Ed.; Springer Nature: Singapore, 2023; pp. 359–374. [[CrossRef](#)]
14. Younis, A.; Dong, Z.; El Badawy, M.; Al Khatib, F.; Al Anazi, A. Development of Low-Speed Wind Energy Harvesting Device. *Energy Rep.* **2022**, *8*, 22–27. [[CrossRef](#)]
15. Chizfahm, A.; Yazdi, E.A.; Eghtesad, M. Dynamic Modeling of Vortex Induced Vibration Wind Turbines. *Renew. Energy* **2018**, *121*, 632–643. [[CrossRef](#)]
16. Bardakjian, A.T.; Mandadakakis, P.P.; Tingle, A. Efficiency Comparison of Horizontal Axis Wind Turbines and Bladeless Turbines. *PAM Rev. Energy Sci. Technol.* **2017**, *4*, 59–75. [[CrossRef](#)]
17. Wang, J.; Geng, L.; Ding, L.; Zhu, H.; Yurchenko, D. The State-of-the-Art Review on Energy Harvesting from Flow-Induced Vibrations. *Appl. Energy* **2020**, *267*, 114902. [[CrossRef](#)]
18. Kawai, H. Vortex Induced Vibration of Circular Cylinder. In Proceedings of the 1st International Symposium on Computational Wind Engineering (CWE 92), Tokyo, Japan, 21–23 August 1992; pp. 605–610. [[CrossRef](#)]
19. Jiménez-González, J.I.; Huera-Huarte, F.J. Vortex-Induced Vibrations of a Circular Cylinder with a Pair of Control Rods of Varying Size. *J. Sound Vib.* **2018**, *431*, 163–176. [[CrossRef](#)]
20. Dol, S.S.; Chan, H.B.; Wee, S.K.; Perumal, K. The effects of flexible vortex generator on the wake structures for improving turbulence. In *IOP conference series: Materials science and engineering*; IOP Publishing: Bristol, UK, 2020; Volume 715, p. 012070.
21. von Kármán, T. Ueber Den Mechanismus Des Widerstandes, Den Ein Bewegter Körper in Einer Flüssigkeit Erfährt. *Nachr. Ges. Wiss. Göttingen Math.-Phys. Kl.* **1911**, *1911*, 509–517.
22. Bearman, P.W. Vortex Shedding from Oscillating Bluff Bodies. *Annu. Rev. Fluid Mech.* **2003**, *16*, 195–222. [[CrossRef](#)]
23. Gerrard, J.H. The Mechanics of the Formation Region of Vortices behind Bluff Bodies. *J. Fluid Mech.* **1966**, *25*, 401–413. [[CrossRef](#)]
24. Su, Z.; Liu, Y.; Zhang, H.; Zhang, D. Numerical Simulation of Vortex-Induced Vibration of a Square Cylinder. *J. Mech. Sci. Technol.* **2007**, *21*, 1415. [[CrossRef](#)]
25. Massai, T.; Zhao, J.; Jacono, D.L.; Bartoli, G.; Sheridan, J. The Effect of Angle of Attack on Flow-Induced Vibration of Low-Side-Ratio Rectangular Cylinders. *J. Fluids Struct.* **2018**, *82*, 375–393. [[CrossRef](#)]
26. Gao, D.; Deng, Z.; Yang, W.; Chen, W. Review of the Excitation Mechanism and Aerodynamic Flow Control of Vortex-Induced Vibration of the Main Girder for Long-Span Bridges: A Vortex-Dynamics Approach. *J. Fluids Struct.* **2021**, *105*, 103348. [[CrossRef](#)]

27. Dol, S.S.; Yong, T.H.; Bin Chan, H.; Wee, S.K.; Sulaiman, S.A. Turbulence Characteristics of the Flexible Circular Cylinder Agitator. *Fluids* **2021**, *6*, 238. [[CrossRef](#)]
28. Khalak, A.; Williamson, C.H.K. Fluid Forces and Dynamics of a Hydroelastic Structure with Very Low Mass and Damping. *J. Fluids Struct.* **1997**, *11*, 973–982. [[CrossRef](#)]
29. Badri, N.; Peddolla, V.; Gottumukkala, H. Design and Analysis of Bladeless Wind Turbine. In Proceedings of the 4th International Conference on Design and Manufacturing Aspects for Sustainable Energy (ICMED-ICMPC 2023), Hyderabad, India, 19–20 May 2023. [[CrossRef](#)]
30. Kim, S.; Alam, M.M.; Sakamoto, H.; Zhou, Y. Flow-Induced Vibrations of Two Circular Cylinders in Tandem Arrangement. Part 1: Characteristics of Vibration. *J. Wind. Eng. Ind. Aerodyn.* **2009**, *97*, 304–311. [[CrossRef](#)]
31. King, R.; Johns, D.J. Wake Interaction Experiments with Two Flexible Circular Cylinders in Flowing Water. *J. Sound Vib.* **1976**, *45*, 259–283. [[CrossRef](#)]
32. Gohate, G.; Bobde, S.; Khairkar, A.; Jadhav, S. Study of Vortex Induced Vibrations for Harvesting Energy. *IJIRST-Int. J. Innov. Res. Sci. Technol.* **2016**, *2*, 374–378.
33. Rishabh, O.; Shubhankar, B.; Vishal, S.K. Bladeless Wind Power Generation. *Int. J. Sci. Eng. Dev. Res.* **2017**, 163–167.
34. Seyed-Aghazadeh, B.; Carlson, D.W.; Modarres-Sadeghi, Y. The Influence of Taper Ratio on Vortex-Induced Vibration of Tapered Cylinders in the Crossflow Direction. *J. Fluids Struct.* **2015**, *53*, 84–95. [[CrossRef](#)]
35. Samy, C.K.; Ahmadi, H.B.; Atfah, Y.A.; Dol, S.S.; Alavi, M. Design of Portable Vortex Bladeless Wind Turbine: The Preliminary Study. *J. Adv. Res. Appl. Mech.* **2023**, *102*, 32–43.
36. Elsayed, A.M.; Farghaly, M.B. Theoretical and Numerical Analysis of Vortex Bladeless Wind Turbines. *Wind Eng.* **2022**, *46*, 1408–1426. [[CrossRef](#)]
37. Akaydin, H.D.; Elvin, N.; Andreopoulos, Y. The Performance of a Self-Excited Fluidic Energy Harvester. *Smart Mater. Struct.* **2012**, *21*, 025007. [[CrossRef](#)]
38. Salvador, C.S.; Teresa, J.A.; Martinez, J.M.; Bacasnot, M.C.; Orilla, K.V.; Cabana, R.J.; Ladaran, W.I. Design and Construction of Arc Shaped and Disc Shaped Pendulum for Vortex Bladeless Wind Generator. In Proceedings of the 25th International Conference on Systems Engineering, ICSEng, Las Vegas, NV, USA, 22–23 August 2017; pp. 363–369. [[CrossRef](#)]
39. Maftouni, N.; Manshadi, M.D.; Mousavi, S.M. The Effect of Drag Force on the Body Frequencies and the Power Spectrum of a Bladeless Wind Turbine. *Trans. Can. Soc. Mech. Eng.* **2021**, *45*, 604–611. [[CrossRef](#)]
40. Francis, S.; Umesh, V.; Shivakumar, S. Design and Analysis of Vortex Bladeless Wind Turbine. *Mater. Today Proc.* **2021**, *47*, 5584–5588. [[CrossRef](#)]
41. Dol, S.S.; Chan, H.B. Fluid-Structural Interaction Simulation of Vortices behind a Flexible Vortex Generator. In Proceedings of the 2019 8th International Conference on Modeling Simulation and Applied Optimization (ICMSAO), Manama, Bahrain, 15–17 April 2019; pp. 1–5. [[CrossRef](#)]
42. Bani-hani, A. Wind Flow Induced Vibrations of Tapered Masts. Ph.D. Thesis, Cleveland State University, Cleveland, OH, USA, 2009.
43. Tandel, R.; Shah, S.; Tripathi, S. A State-of-Art Review on Bladeless Wind Turbine. *J. Phys. Conf. Ser.* **2021**, *1950*, 012058. [[CrossRef](#)]
44. Bahadur, I. Dynamic Modeling and Investigation of a Tunable Vortex Bladeless Wind Turbine. *Energies* **2022**, *15*, 6773. [[CrossRef](#)]
45. Thein, C.K.; Foong, F.M.; Shu, Y.C. Spring Amplification and Dynamic Friction Modelling of a 2DOF/2SDOF System in an Electromagnetic Vibration Energy Harvester—Experiment, Simulation, and Analytical Analysis. *Mech. Syst. Signal Process* **2019**, *132*, 232–252. [[CrossRef](#)]
46. Gatski, T.B.; Bonnet, J.P. *Compressibility, Turbulence and High Speed Flow*, 2nd ed.; Elsevier: Amsterdam, The Netherlands, 2013; pp. 1–328.
47. Menter, F.R. Two-Equation Eddy-Viscosity Turbulence Models for Engineering Applications. *AIAA J.* **1994**, *32*, 1598–1605. [[CrossRef](#)]
48. Yang, Y.; Bremner, S.; Menictas, C.; Kay, M. Battery Energy Storage System Size Determination in Renewable Energy Systems: A Review. *Renew. Sustain. Energy Rev.* **2018**, *91*, 109–125. [[CrossRef](#)]
49. Ould Amrouche, S.; Rekioua, D.; Rekioua, T.; Bacha, S. Overview of Energy Storage in Renewable Energy Systems. *Int. J. Hydrog. Energy* **2016**, *41*, 20914–20927. [[CrossRef](#)]
50. Sridhar, S.; Salkuti, S.R. Development and Future Scope of Renewable Energy and Energy Storage Systems. *Smart Cities* **2022**, *5*, 668–699. [[CrossRef](#)]
51. Sayed, E.T.; Olabi, A.G.; Alami, A.H.; Radwan, A.; Mdallal, A.; Rezk, A.; Abdelkareem, M.A. Renewable Energy and Energy Storage Systems. *Energies* **2023**, *16*, 1415. [[CrossRef](#)]
52. Chavan, S.; Rudrapati, R.; Manickam, S. A Comprehensive Review on Current Advances of Thermal Energy Storage and Its Applications. *Alex. Eng. J.* **2022**, *61*, 5455–5463. [[CrossRef](#)]
53. Rekioua, D. Energy Storage Systems for Photovoltaic and Wind Systems: A Review. *Energies* **2023**, *16*, 3893. [[CrossRef](#)]
54. Rekioua, D.; Rekioua, T.; Elsanabary, A.; Mekhilef, S. Power Management Control of an Autonomous Photovoltaic/Wind Turbine/Battery System. *Energies* **2023**, *16*, 2286. [[CrossRef](#)]
55. Liu, H.; Wang, S.; Zhang, Y.; Wang, W. Study on the Giant Magnetostrictive Vibration-Power Generation Method for Battery-Less Tire Pressure Monitoring System. *Proc. Inst. Mech. Eng. Part C J. Mech. Eng. Sci.* **2014**, *229*, 1639–1651. [[CrossRef](#)]

56. Ueno, T. Performance of Improved Magnetostrictive Vibrational Power Generator, Simple and High Power Output for Practical Applications. *J. Appl. Phys.* **2015**, *117*, 17A740. [[CrossRef](#)]
57. Dey, S.; Roy, D.; Patra, S.; Santra, T. Performance of a Modified Magnetostrictive Energy Harvester in Mechanical Vibration. *Heliyon* **2019**, *5*, e01135. [[CrossRef](#)]

**Disclaimer/Publisher's Note:** The statements, opinions and data contained in all publications are solely those of the individual author(s) and contributor(s) and not of MDPI and/or the editor(s). MDPI and/or the editor(s) disclaim responsibility for any injury to people or property resulting from any ideas, methods, instructions or products referred to in the content.